Improving the Spatial Resolution and Image Noise in Densily Pixilated Detectors for Positron Emission Mammography

Martin J. Hinse

Medical Physics Unit McGill University, Montreal

October, 2004

A thesis submitted to the Faculty of Graduate Studies and Research in partial fulfillment of the requirements of the degree of Master of Science

@2004 by Martin J. Hinse



Library and Archives Canada Bibliothèque et Archives Canada

Published Heritage Branch

Direction du Patrimoine de l'édition

395 Wellington Street Ottawa ON K1A 0N4 Canada 395, rue Wellington Ottawa ON K1A 0N4 Canada

> Your file Votre référence ISBN: 0-494-06403-X Our file Notre référence ISBN: 0-494-06403-X

NOTICE:

The author has granted a nonexclusive license allowing Library and Archives Canada to reproduce, publish, archive, preserve, conserve, communicate to the public by telecommunication or on the Internet, loan, distribute and sell theses worldwide, for commercial or noncommercial purposes, in microform, paper, electronic and/or any other formats.

AVIS:

L'auteur a accordé une licence non exclusive permettant à la Bibliothèque et Archives Canada de reproduire, publier, archiver, sauvegarder, conserver, transmettre au public par télécommunication ou par l'Internet, prêter, distribuer et vendre des thèses partout dans le monde, à des fins commerciales ou autres, sur support microforme, papier, électronique et/ou autres formats.

The author retains copyright ownership and moral rights in this thesis. Neither the thesis nor substantial extracts from it may be printed or otherwise reproduced without the author's permission.

L'auteur conserve la propriété du droit d'auteur et des droits moraux qui protège cette thèse. Ni la thèse ni des extraits substantiels de celle-ci ne doivent être imprimés ou autrement reproduits sans son autorisation.

In compliance with the Canadian Privacy Act some supporting forms may have been removed from this thesis.

While these forms may be included in the document page count, their removal does not represent any loss of content from the thesis.

Conformément à la loi canadienne sur la protection de la vie privée, quelques formulaires secondaires ont été enlevés de cette thèse.

Bien que ces formulaires aient inclus dans la pagination, il n'y aura aucun contenu manquant.



In positron emission mammography, the use of planar detector limits the angular coverage and introduces more noise than conventional positron emission tomography.

We first studied the sampling artifacts introduced from the use of discrete crystals. The images are reconstructed by back-projecting lines of response from and to the centroid of interaction within the crystal. We postulate that the sampling artifact should be reduced by allowing the lines of response to shift away from the centroid towards the next most probable crystal element.

We then studied noise in the peripheral region of the images. The solid angle function is an image uniformity correction function. The solid angle function is the last thing applied before the images are displayed. We postulate that image quality should improve by re-ordering the solid angle function and the smoothing algorithm.

These two techniques have shown an improvement in contrast, resolution, and noise. An ROC curve analysis showed an improvement of 9.5 % in accuracy.

La limite d'angle soutenue par les détecteurs planaires et stationnaires de la mammographie par émission de positrons introduit plus de bruit dans les images que dans ceux de la tomographie par émission de positrons conventionelle.

Dans un premier temps, nous étudions les artefacts d'échantillonnages créés par l'utilisation de cristaux indépendants. Les images sont reconstruites en projetant des lignes de reponses qui commencent et finnissent au centroïde; correspondant au point où l'interaction est la plus probable dans le cristal. Nous postulons que les artefacts d'échantillonnages devraient être réduits en permettant aux lignes de reponses de se déplacer du centroïde vers le second cristal le plus probable.

Dans un deuxième temps, nous étudions le bruit situé à la périphérie des images. La fonction d'angle solide corrige les éfficacités géométriques variables des éléments de l'image et elle est appliquer comme dernière étape de la reconstruction. Nous postulons que la qualité de l'image devrait s'améliorer en ré-organisant l'ordre par laquelle la fonction d'angle solide et le filtre lissant sont appliqué.

Ces deux techniques ont montré une amélioration de l'image au niveau du conntraste, de la résolution et du bruit. Une analyse de courbes ROC a montré une amélioration de 9,5 % en exactitude.

ACKNOWLEGMENTS

I would like to acknowledge my supervisor, Dr. Christopher Thompson for his encouragement, patience, guidance, and generosity during this interesting project. During the many discussions we have had I learned a great deal about all sort of things related and not related to my project.

I would also like to thank my friends at the Montreal Neurological Institute, Nada Tomic, François Cahouette, Nan Zhang, and Ken Nguyen for their friendly attitude in the lab and also my friends at the Montreal General Hospital, Claude, Jason, Vicky, and the others for their encouragement through this intense master degree.

Finally, there is no word that describes how grateful I am towards my girlfriend, Véronique who has been a constant source of encouragement and diversion. This work is dedicated to her and to my son Thomas who is the most beautiful thing that has ever happened to my life.

List of Figures

Figure 2.1	FDG-18 cell cycle.				
Figure 2.2	Illustration of Compton scattering.				
Figure 2.3	Polar plot of the number of 511 keV photons (incident from the left)				
	Compton scattered into a unit solid angle at a scattering angle θ .				
Figure 2.4	Illustration of photoelectric effect.				
Figure 2.5	Interaction importance.				
Figure 2.6	Energy band of an activated scintillation crystal.				
Figure 2.7	Simplified illustration of a photomultiplier tube.				
Figure 2.8	Conventional PET crystal block detector.				
Figure 2.9 Grey scale image of a crystal identification matrix of a 64 crystal					
	block.				
Figure 2.10	Schematic diagram illustrating the construction of a sinogram.				
Figure 2.11	Fundamental factors affecting spatial resolution of a PET scanner.				
Figure 3.1	Illustration of the PEM-1 scanner fitting into a conventional X-ray				
	mammography unit.				
Figure 3.2	Crystal block used in the PEM-1 scanner.				
Figure 3.3	Illustration showing how the DOI is obtained.				
Figure 3.4	Two crystal identification matrices of a BGO crystal block of 10 x 10 and				
	9 x 9 crystal elements for the bottom and the top layer, respectively.				
Figure 3.5	Illustration of the focal plane image formation.				
Figure 3.6	PEM display of a true positive patient.				
Figure 3.7	PEM co-registration image display.				
Figure 4.1	2D LORs drawn for a five crystal elements detector.				
Figure 4.2	Three dimensional histogram of the LOR density through four of the				
	seven image planes.				
Figure 4.3	ROI for crystal element (1, 1, 1).				
Figure 4.4	2D LORs drawn for a five crystal element detector.				
Figure 4.5	Three dimensional histogram of the LOR density through four of the				
	seven image planes.				

- Figure 5.1 Two dimensional illustration of the solid angle subtended by the two different annihilation sites.
- Figure 5.2 Detection probability function or solid angle function for points in a central plane for detector spacing of 50 mm.
- Figure 5.3 Regular and the solid angle reconstruction process.
- Figure 6.1 Graph of the number of patient with and without the disease arranged according to the value of a diagnostic test
- Figure 6.2 Typical ROC curve.
- Figure 7.1 Comparison of the regular identification technique (a) and the sub-crystal identification technique (b) of a contrast phantom experiment.
- Figure 7.2 Comparison of the regular technique (a) and the solid angle technique (b) of a contrast phantom experiment.
- Figure 7.3 Profiles across a point source.
- Figure 7.4 Images of a true positive patient reconstructed using different techniques.
- Figure 7.5 Images of a true positive patient reconstructed using different techniques diagnosed with count asymmetry.
- Figure 7.6 ROC curves from six medical physics students.
- Figure 7.7 Cumulative ROC curves.

List of Tables

Table 2.1	Radionuclides used in positron emission tomography
Table 2.2	Properties of Common Inorganic Scintillators used in PET
Table 6.1	Basic diagnostic test interpretation.
Table 7.1	PEM contrast and SNR for a set of true contrast using the regular and the
	sub-crystal identification.
Table 7.2	PEM contrast and SNR for a set of true contrast using the regular and the
	solid angle technique.
Table 7.3	Spatial resolution and noise for a set of true contrast using the regular and
	the sub-crystal identification.
Table 7.4	Spatial resolution and noise for a set of true contrast using the regular and
	the solid angle technique.
Table 7.5	Accuracy for the two reconstruction techniques

TABLE OF CONTENTS

CHAPTER 1	
INTRODUCTION	1
1.1 Conventional X-ray Mammography	1
1.2 Positron Emission Tomography	2
1.3 Motivation for Positron Emission Mammography	4
1.3 Mouvation for Tostuon Emission Mainingraphy	4
CHAPTER 2	
BASIC PRINCIPLE OF POSTIRON EMISSION TOMOGRAPHY	9
2.1 Radionuclides	10
2.2 Photon Interaction with Matter	11
2.2.1 Compton Scattering	12
2.2.2 Rayleigh Scattering	13
2.2.3 Photoelectric Effect	15
2.2.4 Total Attenuation	17
2.3 PET Detectors	18
2.3.1 Scintillating Crystal	19
2.3.2 Photomultiplier Tube	22
2.3.3 Signal Processing	24
2.3.4 Crystal Identification Matrix	22
2.3.5 Coincidence Detection	25
	23 27
2.3.6 PET Image Formation	28
2.3.7 Spatial Resolution in PET	28
CHAPTER 3	
POSITRON EMISSION MAMMOGRAPHY SYSTEM	32
3.1 Detectors	32
3.2 Crystals and PMTs	33
3.3 Data Aquisition and Image Formation	37
3.4 Image Display	39
3.4 image Display	39
CHAPTER 4	
UNDER-SAMPLING ARTIFACTS	41
4.1 Determination of Centroid of Interaction	41
4.2 Sampling Artifacts	42
4.3 Energy Deposition in Crystal	46
4.4 Sub-Crystal Identification	46
·	
CHAPTER 5	
SOLID ANGLE FUNCTION	52
5.1 Detection Probability	53
5.2 Solid Angle Function	56
5.3 Re-Ordering of the Solid Angle and the Smoothing Algorithm	57

CHAPTER 6	
QUANTITATIVE ANALYSIS	60
6.1 Breast Phantom Study	60
6.2 Point Source Study	62
6.3 Clinical Trial Study	62
6.4 ROC Curve Analysis	63
CHAPTER 7	
RESULTS	68
7.1 Contrast Phantoms Measurements	68
7.2 Point Source Measurements	73
7.3 Clinical Trial Replay	76
7.4 RO Curve Analysis	80
CHAPTER 8	
DISCUSSION AND CONCLUSION	83
APPENDIX	87
REFERENCES	89

CHAPTER 1

Introduction

Breast cancer is the most frequent malignant disease and it has the second leading cause of cancer death in western countries. During the year 2003 in Canada, 21 100 women were diagnosed has having breast cancer and 5300 died of the disease. About one in nine women is expected to develop breast cancer in her lifetime, and one in 27 is expected to die of the disease. Self examination, routine breast examinations, and screening modalities like X-ray mammography along with a better understanding of the biology of breast cancer, have reduced the age-standardized mortality rate of breast cancer by about 5 % in the past 30 years even if the age-standardized occurrence rate has increased by about 20 % in the same time period [1].

1.1 Conventional X-ray Mammography

X-ray mammography is the screening technique mostly used for the detection of breast cancer. Conventional X-ray mammography identifies microcalcifications and abnormal breast masses in 80 – 90 % of the cases in which breast cancer is truly present [2, 3] but unfortunately benign tissue alterations often display similar image appearances and only 15 - 35 % of the apparently positive X-ray findings are really breast cancer [4, 5]. This leads to many unnecessary invasive procedures like needle biopsy, aspiration cytology, core needle biopsy, or incisional or excisional biopsy followed by histological examination of the excised tissue. Conventional X-ray

mammography is therefore a high sensitivity but low specificity screening device. Early detection has shown to decrease the death rate in recent years but a reduced accuracy is found in younger women or women with dense breast [6]-[8]. Clearly there is a need for a better screening modality for breast cancer which should have:

- 1. High sensitivity to tumor detection, especially the early stage cancer, since curability is increased with early detection.
- 2. High specificity leading to an accurate differentiation between malignant and benign masses.
- 3. Non invasive procedure.
- 4. Easy to use.
- 5. Reasonable cost.

1.2 Positron Emission Tomography

Positron emission tomography (PET) is a metabolic imaging modality that uses a radiopharmaceutical to detect increase metabolic rate of malignant cells. The radiopharmaceuticals used for PET are positron emitters. The positron encounters an electron and since they are antiparticle of each other, they annihilate emitting two antiparallel gamma-rays. Many gamma-ray detectors are positioned in a ring around the patient and coincidence detection of two gamma rays is kept as a count. Images of radiotracer distribution are reconstructed using tomographic techniques. These images are used to find where in the body the radiotracer accumulated.

Many different studies have clearly showed that the radiolabeled glucose analogue ¹⁸F-fluorodeoxyglucose PET, or FDG-PET, is an excellent clinical method for the detection of breast cancer [9]. A large study conducted by Avril et al. [10] with 144 patients scheduled for a subsequent histological tissue examination showed promising clinical results using PET for the diagnosis of breast cancer. The images were analyzed for increased tracer uptake applying conventional image reading (CIR) and sensitive image reading (SIR). The study published an overall sensitivity of 64 % and 80 %, and a specificity of 94.3 % and 75.5 %, for CIR and SIR respectively. They stated a diagnosis accuracy of 68 % for early stage pT1 to 92 % for later stage pT2 and approaching 100 % for large tumor of stage pT3. Their results clearly showed the dependence of diagnosis accuracy on tumor size.

Other studies conducted on smaller groups showed even more promising results. Another study done by Scheidhauer et al. [11] performed with 30 patients found a sensitivity of 91 % and a specificity of 86 %. One study performed by Adler et al. [12] on 28 patients found a sensitivity of 96 % and a perfect specificity of 100 %. Other studies performed by Wahl et al. [13], Tse et al. [14], Nieweg et al. [15], and Bruce et al. [16] of about 10 to 15 patients each have published sensitivities of 93 ± 6 % and all got a specificity of 100 %.

1.3 Motivation for Positron Emission Mammography

FDG-PET has a high sensitivity, a good specificity providing a much higher accuracy than conventional X-ray mammography. Even if PET facilities are becoming much more numerous, they are still quite rare and too expensive for routine use in the diagnosis of breast cancer.

FDG production is facilitated with cyclotron present in most big cities. The two hour half life of fluorine-18 (F-18) makes it a suitable radioisotope for distribution to several sites within a city. This makes FDG a readily available source if another smaller, easier to use and cheaper PET camera design for breast imaging were available in clinics.

Precise co-registration is important in diagnostic imaging. It permits a good identification, localization, and quantification of change from one modality to the next. Until recently PET co-registration with computed tomography (CT) imaging was a big challenge. Sophisticated software algorithms were developed to perform image fusion of the two modalities but apart from the brain the alignment is quite difficult and often unsuccessful due to organ motion between the two scans. This time consuming practice is far from routine in most clinical centers. With the arrival of the PET-CT scanner [17]-[19], co-registration is now very easy and precise since the two images are taken almost simultaneously. In 2001, the PET/CT scanner, attributed to Dr David Townsend, professor of radiology and senior PET physicist at the University of

Pittsburgh, and Dr Ronald Nutt, President of CPS Innovations, was named the medial invention of the year 2000 by TIME Magazine.

One great advantage of PET/CT is the use of the CT data for attenuation correction [20]. Regular PET images need to be corrected for photon attenuation. For 3-D PET imaging, the attenuation correction is usually done by imaging in coincidence mode with a low activity ⁶⁸Ge rod source. The 511 keV annihilation photons from ⁶⁸Ga are detected during a transmission seen as the source rotates around the patient. Since the CT images are maps of attenuation factors across the patient, an alternate approach in PET/CT is the use of CT based attenuation correction. This process saves time and is much more precise than the rod source technique.

However the detection of breast cancer using PET/CT is restricted by the relatively low spatial resolution of CT which prevents the identification of micro calcifications compared with conventional X-ray mammography.

Therefore a device combining PET and X-ray mammography would be a modality of choice for the detection of breast cancer. The device would take advantage of the high sensitivity of conventional X-ray mammography and the high specificity of PET. It should be suited for breast cancer, in that it should have a higher spatial resolution than PET and the same X-ray spatial resolution as conventional mammography. The device should be inexpensive, easy to use and the scan time should be kept short as to reduce personnel costs and justify its use.

In the past several years, the development of positron emission mammography devices, commonly referred as PEM, has started in many research centres. Different PEM detector designs have been proposed by many groups [21]-[25]. Most of them use two planar detectors facing each other and finely pixilated scintillating crystals. The simplest PEM image reconstruction method consists of back-projecting lines-of-response (LORs) onto several virtual planes located in between the two detectors [26]. It was shown that an iterative reconstruction algorithm, like the one proposed by Huesman et al. [27], produces better results [28]. However the back-projection method is still used since it can be performed in real time contrarily to the iterative technique that can take several hours to converge. Initial clinical results have showed excellent results with an increase accuracy in imaging small lesions in breast compared with PET or X-ray mammography alone [29]-[31].

PEM differs from PET in the geometric configuration. To allow an image of the whole-body, PET requires a ring of detectors located around the patient. The ring is made of a certain diameter to accommodate different size patient or different scan position. PEM on the other hand has the sol purpose of imaging the breast and therefore is made to come very close to the breast. The detectors where actually chosen to be planar and moveable so to compress the breast as in conventional X-ray mammography. In most cases, the detectors have much less then 30 cm of separation and therefore have better geometrical efficiency compared with whole-body PET scanners. Brain PET scanners can have a much smaller diameter and normally much

more detector rings than whole body PET scanners but is still a short distance from the head and therefore does not have as high of a solid angle coverage has PEM.

The fact that the detectors are compressing the breast reduces the image blurring caused by the non-colinearity of the two gamma rays emitted from the positron annihilation. The compression also reduces the probability that photons will scatter in the breast but more of these scattered photons are detected due to the high solid angle coverage.

PEM-1 was developed in our lab at the Montreal Neurological Institute of McGill University, Montreal, Qc, Canada [24]-[26]. It has two movable planar detectors so that the breast can be compressed as in a normal mammography unit. Our design is similar to PET-CT in that the device is integrated to a conventional X-ray mammography unit for co-registration [32]. In 1997 a clinical trial was conducted by our group with PEM-1. On a total of 16 cases studied, 10 cancerous tumors and four benign lesions were confirmed after complete removal of the tumor. The images for the two other patients were not valuable. From this initial trial we reported an accuracy of 86%, a sensitivity of 80%, and a specificity of 100% for the PEM-1 [31]. During the clinical trial of our PEM-1 instrument we observed more noise in the peripheral regions of the images than could be accounted for by Poisson counting statistics.

In this thesis we tested two techniques to address problems of sample density artifacts and noise near the edges PEM images which should improve image quality.

We also verified if the accuracy of PEM-1 could improve with a receiver operator characteristic (ROC) analysis.

CHAPTER 2

Basic Principles of Positron Emission Tomography

PET is commonly used as a metabolic image technique that can detect increased in metabolic rate of malignant tumors through the introduction of a radioisotope into the body. The radioisotope is usually attached to a specific molecule to produce a radiopharmaceutical which acts as a tracer. An appropriate tracer will preferentially be absorbed by active cancerous cells than by cells with normal metabolism. The radiopharmaceutical will also distributed in the body through the blood and accumulate into organs that consume that specific molecule. Contrarily to computed tomography (CT) which produces an anatomical image of the patient with the help of an external highly collimated X-ray beam, PET produces a functional image of the patient.

Table 2.1 Radionuclides used in positron emission tomography

Radioisotope	Maximum positron energy	$\mathrm{T}_{1/2}$	Maximum range in water
¹⁵ Oxygen	1.72 MeV	2.0 min	8.0 mm
¹³ Nitrogen	1.19 MeV	10.0 min	5.4 mm
¹¹ Carbon	0.96 MeV	20.4 min	4.1 mm
¹⁸ Fluorine	0.69 MeV	109.8 min	2.4 mm

2.1 Positron Emission and Annihilation Photons

All radioisotopes used in PET are positron emitters. Positrons are emitted from nucleus with an excess in protons. These isotopes are produced by bombarding a target, i.e. a non radioactive element like oxygen-18, with a beam of high energy protons accelerated with a cyclotron. Table 2.1 shows some characteristics of a few radioisotopes used in PET. Table 2.1 shows the maximum positron energy, the half life of the isotope, and the average range of the emitted positron in water.

The unstable nucleus will decay through positron decay. In positron decay, a proton is transformed into a neutron. Since charge and parity are conserved, a positron and a neutrino are emitted from the decay; hence the name positron decay. While the neutron stays bounded to the nucleus, the positron is ejected from the nucleus.

The emitted positron travels a short distance loosing most of its kinetic energy through inelastic collisions with electrons of the surrounding tissue. When almost completely stopped, the positron forms a very unstable nucleus called positronium with a loosely bound electron. The two particles annihilates emitting two 511 keV gamma rays. From conservation of energy and momentum the two gamma rays will be emitted 180 degrees from each other.

2.2 FDG

FDG-18 or simply FDG stands for fluorodeoxyglucose-18, it is a glucose analog molecule to which is attached a radioactive atom of fluorine-18. FDG has been shown to be a suitable tracer to study the increase glucose consumption of malignant

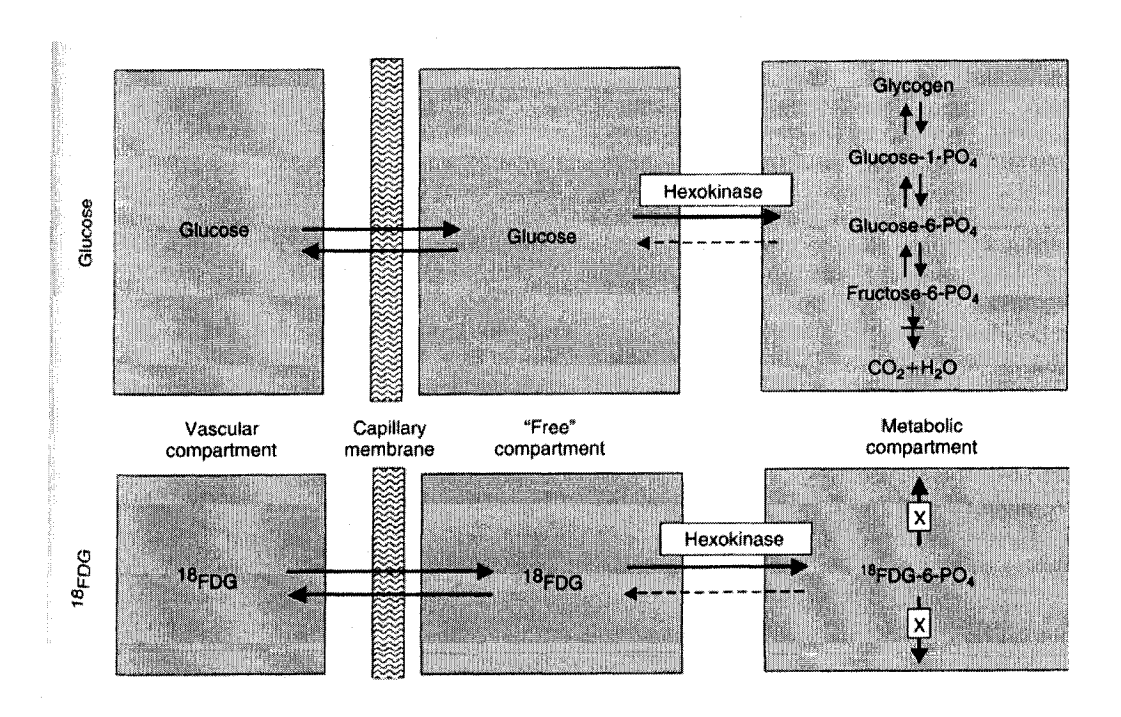


Figure 2.1 FDG-18 cell cycle. The figure was taken from Cherry et al [32].

tumors and is now the most common radiopharmaceutical used in PET [32].

As opposed to the normal glucose cycle, FDG doesn't go through the whole glucose metabolic cell cycle. FDG is transferred from the blood to the cell and makes ¹⁸FDG-6-PO₄ which remains trapped in the cell (Figure 2.1). The active cancerous cells which consume more glucose than regular cells will absorb more FDG. In addition, proliferating cancerous cells are also hypoxic and in the absence of oxygen they can redirect the vessels around them for a better oxygen and glucose provisioning. Therefore, proliferating cells have a much higher FDG uptake [32].

2.2 Photon Interactions with Matter

The two gamma-rays travel through the body and need to be detected in coincidence with detectors located outside the body. The annihilation gamma ray can interact with matter through various interaction mechanisms. Three major types play an important role in PET and they are: Compton scattering, Rayleigh scattering and photoelectric effect. These interactions are classified in two fundamental categories: elastic or inelastic interactions. Elastic collision, like Rayleigh scattering, leads to no change in energy but a possible change the photon's direction of propagation. Inelastic collision, like Compton scattering or photoelectric effect, leads to a partial or complete transfer of the gamma ray energy to electron energy. While pair production is another possible interaction mechanism, the 511 keV annihilation photon has an insufficient energy to trigger the interaction.

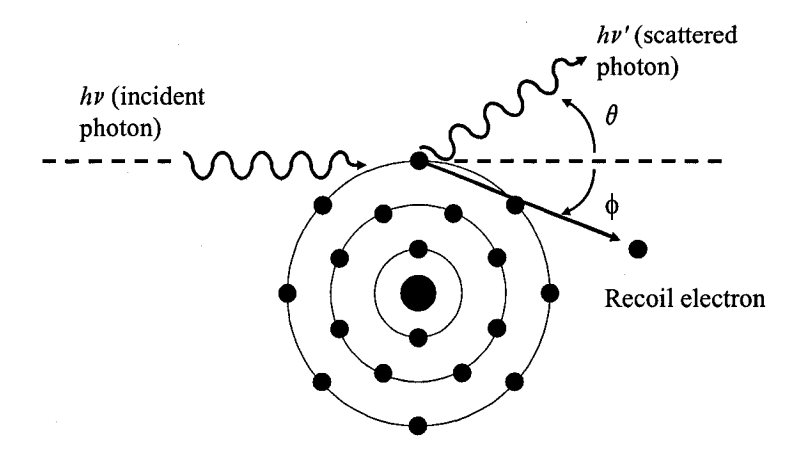


Figure 2.2 Illustration of Compton scattering.

2.2.1 Compton Scattering

Compton scattering is an interaction between the gamma ray and an atomic 'free' electron. An atomic free electron is an electron whose binding energy is much less than the gamma ray energy. In Compton scattering, some of the photon energy is transferred to the electron which is ejected from the atom with angle θ . The photon is also scattered at an angle ϕ as illustrated by Figure 2.2.

From conservation of energy and momentum, one can derive the following relationships.

$$E = hv \frac{\varepsilon(1 - \cos\phi)}{1 + \varepsilon(1 - \cos\phi)}$$
 (2.1)

$$hv' = hv \frac{1}{1 + \varepsilon(1 - \cos\phi)} \tag{2.2}$$

where $h\nu$, $h\nu'$, and E are the energy of the incident photon, the energy of the scattered photon and the energy of the recoil electron, respectively and, $\epsilon = h\nu/m_o c^2$, where $m_o c^2$ is the rest energy of the electron (511 keV).

The angular distribution of scattered gamma rays is predicted by the *Klein-Nishina formula* for the differential scattering cross section $d\sigma/d\Omega$.

$$\frac{d\sigma}{d\Omega} = Zr_0^2 \left(\frac{1}{1+\varepsilon(1-\cos\theta)}\right)^2 \left(\frac{1+\cos^2\theta}{2}\right) \left(1+\frac{\varepsilon^2(1-\cos\theta)^2}{(1+\cos^2\theta)[1+\varepsilon(1-\cos\theta)]}\right)$$
(2.3)

Figure 2.3 shows the distribution for gamma ray energies of 25, 511, and 10000 keV normalized to one for 0°. The distribution is Figure 2.3 illustrates the preference of higher energy photons for forward scattering.

The probability for Compton scattering to occur increases with the number of available free electrons and therefore increases linearly with atomic number. The probability decreases gradually with increasing photon energy.

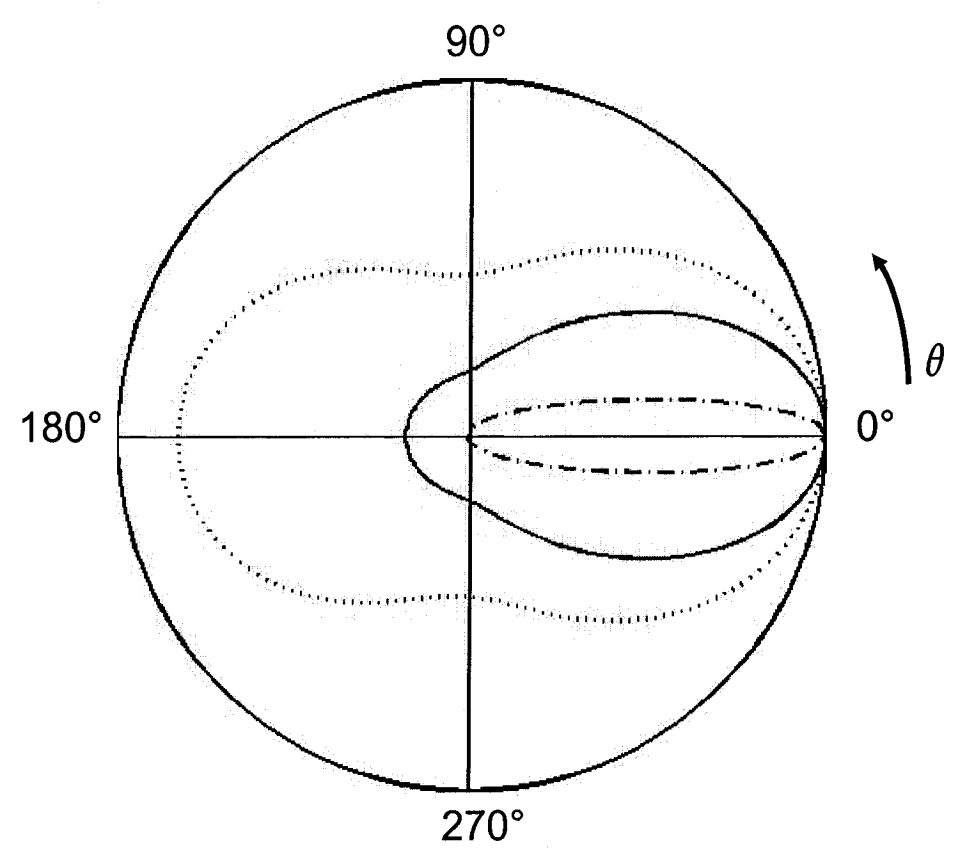


Figure 2.3 Polar plot of the number photons (incident from the left) Compton scattered into a unit solid angle at a scattering angle θ . The solid line is for 511 keV photons, the dotted line is for 25 keV photons, and the dash-dotted line is for 10 MeV photons.

2.2.2 Rayleigh Scattering

Rayleigh scattering, also known as classical scattering or coherent scattering, consist of the interaction of a photon with all the electrons of the atom. The interaction is coherent meaning that the photon preserve its energy and hence its wavelength after the interaction. Thus not energy is absorbed in the medium. The only effect is the scattering of the photon at a small angle. Rayleigh scattering is mostly important in materials with high atomic number and with photons of low energy and is therefore negligible in PET.

2.2.3 Photoelectric effect

The photoelectric effect is an inelastic collision between a photon and an atom. The photon completely disappears, transferring all of its energy, and a photoelectron is ejected from the atom. The photoelectron's kinetic energy KE_e will be:

$$KE_e = h \nu - E_B \tag{2.4}$$

where E_b is the binding energy of the photoelectron in its original shell. Photoelectric effect creates a vacancy in the K, L, M, or N shell and leaves the atom in an excited state. This vacancy is filled by an outer orbital electron with the emission of characteristic X-rays. The other possibility for the atom to de-excite is the emission of an Auger electron. The probability for Auger electron decreases with increasing atomic number.

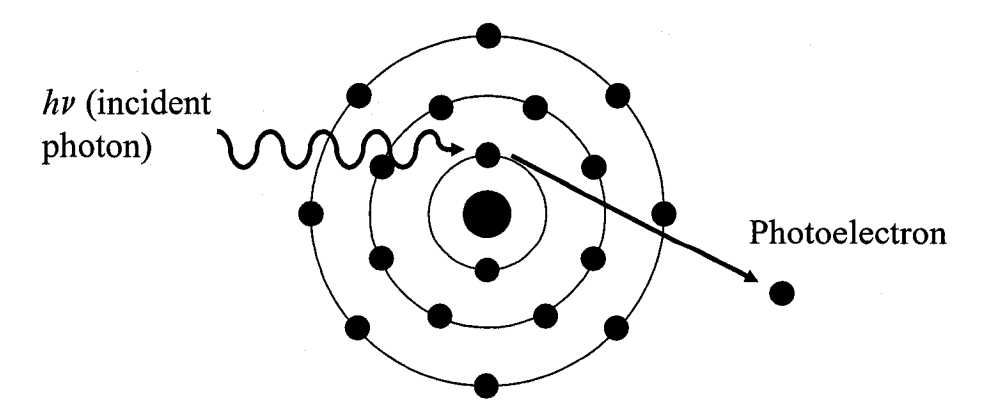


Figure 2.4 Illustration of photoelectric effect.

Photoelectric effect becomes most probable for photon energies equal or slightly higher then the binding energy of the electron. Photoelectric effect strongly depends on both the energy of the incident photon and the atomic number of the absorbing material. As in Compton scattering, photoelectric effect decreases with increasing photon energy and increases with increasing atomic number. The following approximate relationship holds between the mass photoelectric attenuation coefficient τ/ρ , the atomic number Z, and the photon energy $h\nu$:

$$\frac{\tau}{\rho} \propto \frac{Z^3}{(h\nu)^3} \tag{2.5}$$

That relationship forms the basis of X-ray imaging. The difference in atomic number between bone, muscle, and lung provides high contrast at low X-ray energies. Megavoltage imaging is performed in radiotherapy but the images have bad contrast. It is only used for positioning before treatment.

Figure 2.5 shows the relative importance of photoelectric effect, Compton effect, and pair production for different photon energies and atomic number material. As told before for a 0.511 MeV photon, pair production is not a possible interaction.

2.2.4 Total Attenuation

Overall, if all photon interactions are considered, a photon beam is exponentially attenuated. For a piece of material of thickness x placed in a beam of N_0 incident photons, the attenuation equation is [33]:

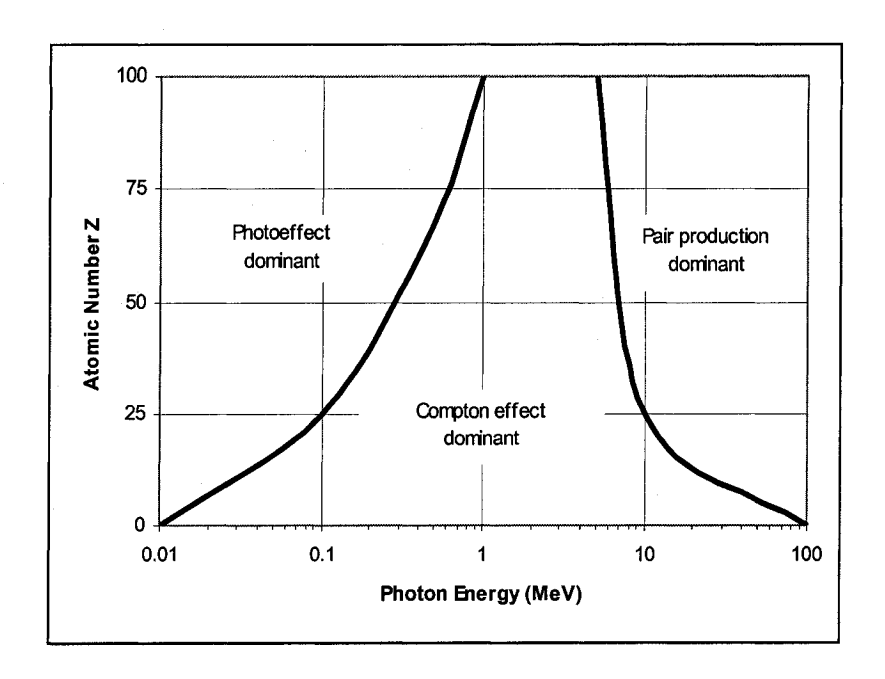


Figure 2.5 Interaction importances. This graph was obtained by plotting data from Podgorsak [33].

$$N(x) = N_0 e^{-\mu x} {2.6}$$

where N(x) is the number of photons transmitted through a thickness x and μ is the total linear attenuation coefficient. For 511 keV annihilation photons in bismuth germanate (BGO) which is a type of scintillating crystal used in PET (discussed in the next sections), the attenuation coefficient is $\mu = 0.92$ cm⁻¹. So the half value layer (HVL) of BGO for a 511 keV photon beam is 0.75 cm [35].

2.3 PET Detectors

The PET detectors are normally made of a combination of a scintillating crystal block and a photo-multiplier tube (PMT). In a whole body PET scanner, detectors are positioned around the patient into a ring of detectors. For example the

PET scanner ECAT EXACT HR⁺ (Siemens/CTI, Knoxville, TN, USA) has four rings of detectors of 80 crystal blocks. Each crystal block is optically coupled to 4 PMTs.

2.3.1 Scintillating Crystal

Scintillation materials are used in the detection of gamma rays emitted from the positron annihilation. The gamma ray energy is transferred to the scintillation material through Compton scattering and photoelectric effect and the energy is then re-emitted into visible light photons. The ideal scintillation material should have the following properties:

- 1. High atomic number and density.
- 2. Convert the kinetic energy of charged particles into detectable light with high scintillation efficiency.
- 3. The light yield should be linear, i.e. amount of light should be proportional to the amount of deposited energy.
- 4. The material should be transparent to its own light photon emission.
- 5. The light decay should be short in order to detect consecutive gamma rays.
- 6. For good optical coupling with the PMT, the index of refraction of the material should be close to that of glass.
- 7. Low cost production.

No scintillation material meets all of those criteria and so the selection of a particular scintillation over another is often a compromise between different factors such as; experimental requirements, availability, and monetary resources.

Table 2.2 shows some characteristics for three types of inorganic scintillation materials used in nuclear medicine and PET [35]. The table includes thallium activated sodium iodine (NaI(Tl)), bismuth germanate (BGO), and cesium activated lutetium oxyorthosilicate (LSO).

Table 2.2 Properties of Common Inorganic Scintillators used in PET

Scintillators	NaI(Tl)°	BGO*	LSO [†]
Hygroscopic	Yes	No	No
Relative Light Output	100	15	75
Scintillation Decay Time (ns)	230	300	40
Refractive Index	1.85	2.15	1.82
Wavelength of Max. Emission (nm)	415	480	420
Density (g/cm3)	3.67	7.1	7.4
Effective Atomic Number	51	75	66
Total Linear Attenuation (cm ⁻¹)	0.34	0.92	0.87

[°] Thallium activated sodium iodine

^{*} Bi₄Ge₃O₁₂ or bismuth germanate

[†] Lu₂(SiO₄)O or lutetium oxyorthosilicate

Figure 2.6 shows the scintillation mechanism for inorganic scintillation crystal. The valence band represents the electrons that are bound to the lattice sites, whereas the conducting band represents those electrons that are free to migrate throughout the crystal lattice. Gamma rays interacting with the crystal transfer energy that is used to free electrons in the valence band and creating wholes that must be filled in the valence band. With the help of impurities, also called activators, added to inorganic scintillation crystal, the electrons will fall back to the valence band through energy states created within the forbidden band. The band gaps created within the forbidden band by the activator are such that visible scintillation photons are emitted when a transition occurs. These number of light photons emitted will be proportional to the energy transferred form the incident gamma rays into the crystal.

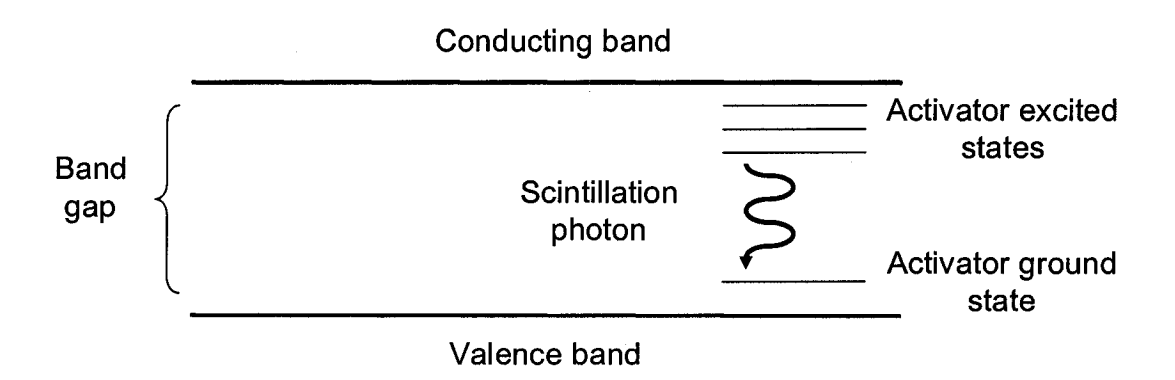


Figure 2.6 Energy band of an activated scintillation crystal.

2.3.2 Photomultiplier tube

A photomultiplier tube (PMT) is a device used to convert a light signal into a corresponding electrical signal. PMTs can detect the weak light output from scintillation crystals and output a usable current pulse.

Figure 2.7 PMT shows the simplified structure of a PMT. A light photon from the crystal enters the vacuum tube through the entrance window before striking the photocathode. The photocathode is used to convert the incident photon into an electron through photoelectric processes. An electric field is used to attract the photoelectron to the first of a series of dynodes. The dynode, when struck by the photoelectron, will reemit about four electrons that will be attracted to the next dynode which is at an even

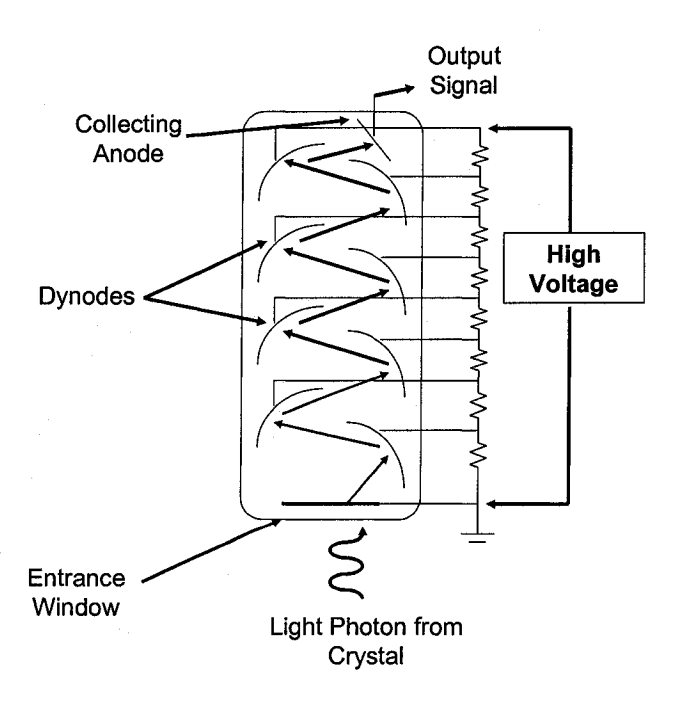


Figure 2.7 Simplified illustration of a photomultiplier tube.

greater potential. The increasing potential in the series of dynodes is obtained using a voltage divider. A voltage divider is simply a series of resistors connected to a high voltage. After amplification through the multiplier structure, the gain in electrons will be approximately 10⁶. Those electrons are collected at the anode and form the output signal. The output signal height will correspond to the total number of electrons collected at the anode which is related to the number of photoelectrons emitted by the photocathode. This conversion is done, for most PMTs, in a very linear fashion, so that the output signal stays proportional to the amount of light photons that enters the PMT over a wide range of photon flux. The process is a very fast one; a PMT will produce an electron pulse in a few nanoseconds.

In PET we are interested in the scintillation photon counting; we want to know how much energy was deposited in the crystal. The height of the output pulse will determine the energy of the incident radiation. A unit of great interest is the quantum efficiency (QE), which is the ratio of the number of photoelectron emitted over the number of incident photons. The spectral response characterizes the QE of the PMT as a function of wavelengths. Therefore the choice of a particular PMT is done by matching the spectral response of the PMT with the wavelength of the scintillation photons emitted by the crystal.

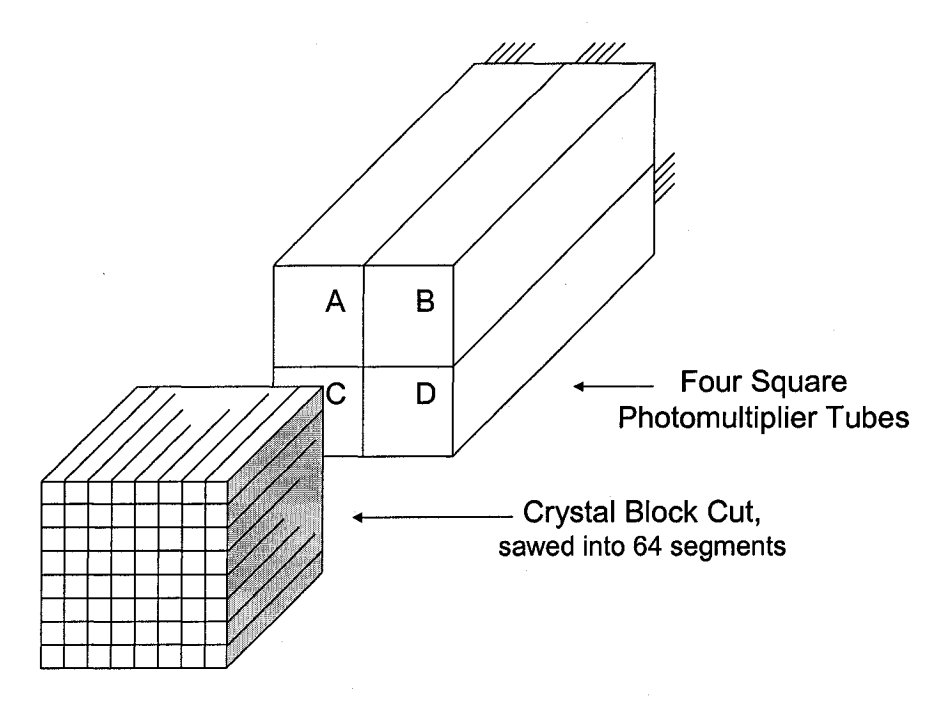


Figure 2.8 Conventional PET crystal block detector.

2.3.3 Signal processing

A schematic diagram of a most conventional PET detector is shown in figure 2.8. Four PMTs are coupled to a BGO or LSO crystal block which is sawed into an array of 64 crystal elements.

The only independent crystal elements in that geometry are the ones at the four corners. The other crystal elements are all in contact with the same crystal block. The configuration is known as "Anger Logic". The raw positions, X and Y, and the energy E of the annihilated photon are determined from the four hardware signals of the PMTs; A, B, C, and D. They are given by the following equations:

$$X = \frac{(B+D) - (A+C)}{A+B+C+D}$$
 (2.7)

$$Y = \frac{(A+B) - (C+D)}{A+B+C+D} \tag{2.8}$$

$$E = A + B + C + D \tag{2.9}$$

These three signals are usually digitized with an eight bit analog to digital converter (ADC) and sent to the computer if the energy is between the upper and lower energy discriminator settings. The energy has to be within a certain window, set by the user, representing full energy deposition of a 511 keV photon.

2.3.4 Crystal Identification Matrix

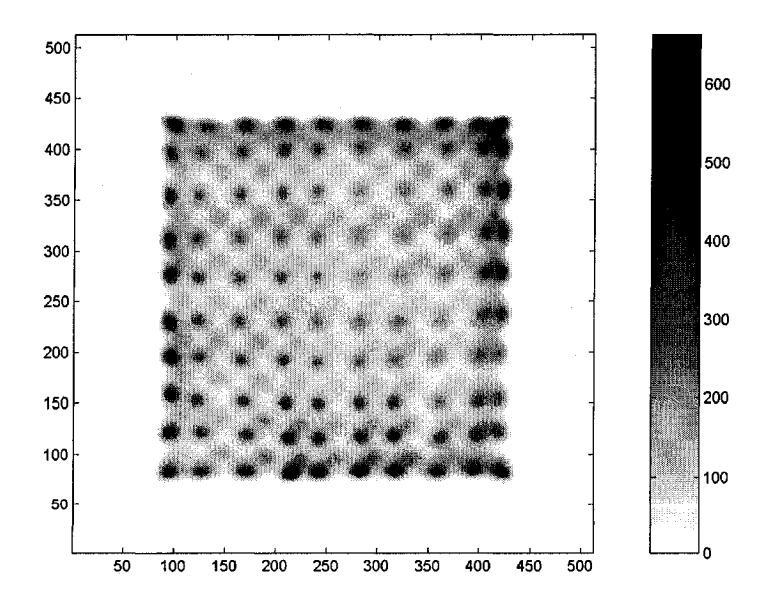


Figure 2.9 Grey scale image of a crystal identification matrix of a 10×10 and 9×9 two layers crystal block from Zhang et al. [25].

The X and Y raw positions obtain from Anger logic are stored into a crystal identification matrix. The crystal identification matrix is required to map, at the software level, the (X, Y) raw hardware coordinates from the PMTs onto elements of the cut crystal array. The crystal identification matrix corrects for the spatial distortion introduced by the use of PMTs. Figure 2.9 shows a crystal identification matrix [25].

The crystal identification matrix is obtained by irradiating the detector face with a point source located far enough as to produce a uniform flood irradiation. Once enough counts are collected, the crystal identification matrix is obtained by plotting a two-dimensional histograms of (X, Y) raw positioning pairs.

Regions of interest (ROI) are drawn around each blob in the crystal identification matrix. Each ROI therefore correspond to one crystal element of the block. These regions are then stored into a distortion look-up-table (LUT) that is further used in a real scan to find into which of the crystal elements in the block the photon interacted with. The distortion LUT is a two-dimensional (256 x 256) matrix with its value corresponding to one crystal element.

2.3.5 Coincidence Detection

As previously discussed, the emission of two anti-parallel 511 keV gamma rays follows the decay of a positron emitting radioisotope. The aim of PET is to detect both gamma rays in coincidence. In practice, uncertainties created by the scintillation crystal, the PMTs, the hardware, and the time taken for the photon to cross the field of

view will make it impossible to detect coincidence events with 100 % accuracy. A hardware coincidence device determines when two events are in coincidence allowing a maximum time difference between two events called the coincidence resolving time. The coincidence resolving time, usually represented by τ , is strongly dependent on the scintillation light decay of the type of scintillation crystal used. As seen in Table 2.2, an LSO crystal is much faster than a BGO crystal and will be able to have a shorter resolving time. Typical resolving times are of the order of 6 to 16 ns for whole-body PET scanners.

2.3.6 PET Image Formation

In PET, one count corresponds to the detection of two annihilation photons in coincidence. All counts are stored into arrays called sinograms. Sinograms are also used in computed tomography and are most suitable for direct use by conventional image reconstruction algorithms.

Figure 2.10 is an illustration showing where a coincidence at a certain position inside the detector ring would go into the sinogram. The horizontal coordinate of the sinogram represents the distance from the line of response (LOR) connecting the two detectors to the center of the ring of detectors, r, and the vertical coordinate of the sinogram represents the angle made by the normal to the LOR and the horizontal axis of the detector ring, θ . The sinogram is a two-dimensional histogram where each rows correspond to one projection of the patient at a certain angle.

The filtered back projection (FBP) algorithm and statistical model based iterative algorithms such as ordered-subset expectation maximization (OSEM) reconstruction are the two major classes of tomographic reconstruction methods used in PET. Maximum likelihood (ML) reconstruction are known to perform better with respect to image quality but take more time to produce the images. Hence the FBP algorithm is mainly used in clinical settings, where time is precious, while ML is

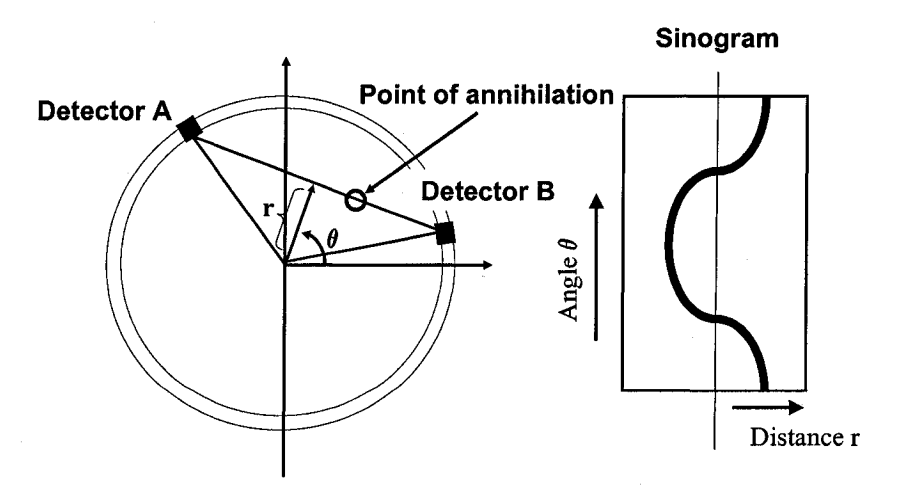


Figure 2.10 Schematic diagrams illustrating the construction of a sinogram. A point of interaction positioned at r from the centre of the scanner would trace a vertical sinus curve of amplitude r into the sinogram.

mostly used in research settings where time is not a key factor. Tomographic image reconstruction has been an active research field in past few years and is still very active. Many different algorithms have been design and tested on different types of PET images. Even if this thesis discusses problems and improvements in PEM image formation, it is not mandatory neither necessary to dwell on a detailed explanation of tomographic reconstruction algorithms used in PET.

2.3.7 Spatial Resolution in PET

Spatial resolution of a PET scanner is fundamentally affected by five factors. These are the positron range, the photon noncolinearity, the detector crystal width, the block effect and the reconstruction algorithm used. They are illustrated in Figure 2.11 which was taken from a presentation giving by W. W. Moses.

As previously mentioned, from energy and momentum conservation, the positron emitted from positron emitting radioisotopes, will have some extra kinetic energy which will be lost through inelastic collisions with electrons inside the patient. The positron will travel a certain overall distance that will affect spatial resolution since the two annihilation gamma rays will be emitted a short distance away from the original decay site. F-18 produces a low-energy positron which doesn't travel far before annihilating and thus results in a spatial resolution degradation with a full width half maximum (FWHM) of about 0.2 mm [37]. The maximum positron ranges are shown in Table 2.1 for different radioisotopes.

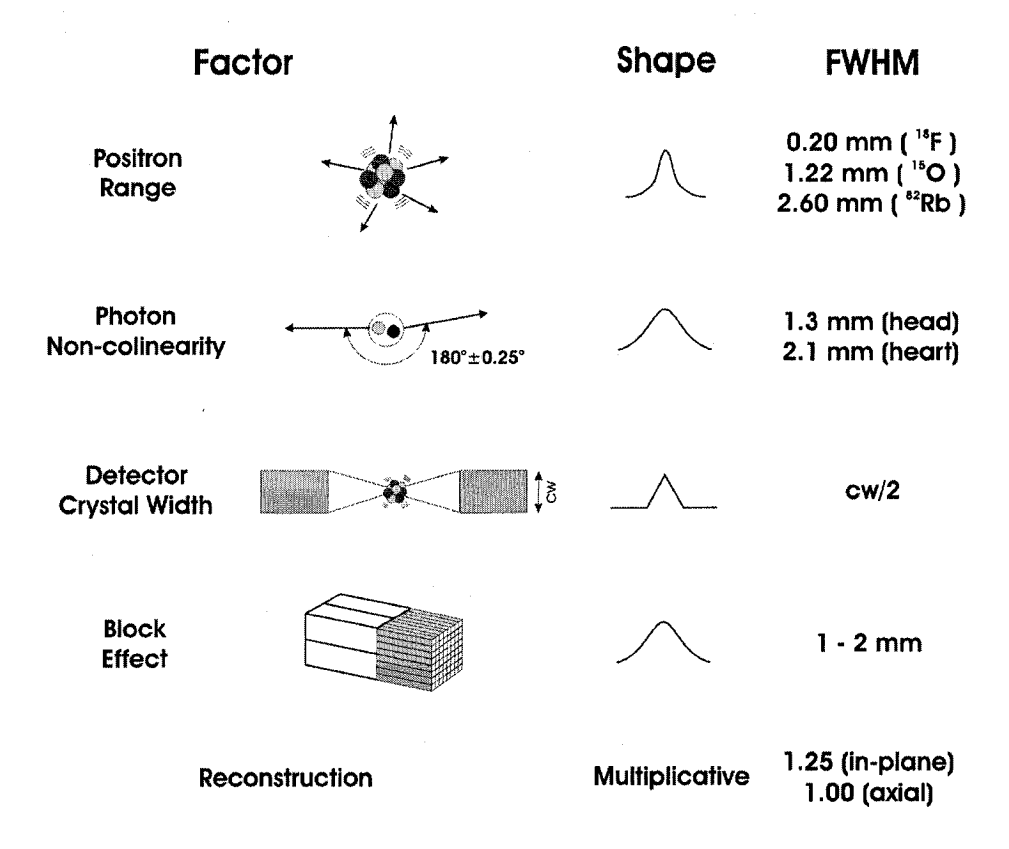


Figure 2.11 Fundamental factors affecting spatial resolution of a PET scanner.

The photon noncolinearity is also a spatial resolution degradation effect caused the motion of the centers of masses of the annihilating electrons and positrons. From that process the annihilation photons will not be emitted with precisely 180 degrees between them. The angular deviation is represented by a Gaussian distribution with FWHM of about 0.5 degrees for most positron emitters and materials [38]. The lost in spatial resolution from photon noncolinearity increases with detector separation. A regular PET scanner with a separation of 100 cm will have an effect of about 2 mm on the FWHM.

The size of the crystal is also a factor affecting spatial resolution. One would expect using very thin and closely pack crystal elements would decrease that effect.

Unfortunately reducing the crystal size reduces gamma ray detection efficiency and increases cross talk between neighbouring crystal elements. The effect on spatial resolution is equal to d/2 FWHM where d is the crystal element width.

The use of block detectors is believed to have an effect on spatial resolution as well. Nada Tomic [39], a colleague in the MNI lab, has studied that effect in great depth and found that it had a much smaller effect than previously suggested by Moses et al. [40]. The results of Tomic from an experiment specifically design to measure the block effect by precisely determining the other factors effect, showed that there was a block effect of FWHM equal to 1.1 mm for block detectors in coincidence. This result is significantly different from a previously reported value of 2 mm by Moses et al which suggest that there are other factors affecting spatial resolution.

Overall the spatial resolution (SR) in mm of a PET scanner can be calculated using [40]:

$$SR = 1.25\sqrt{\left(\frac{d}{2}\right)^2 + (0.0022 \cdot D)^2 + s^2 + b^2}$$
 (2.10)

where d is the crystal width, D is the diameter of the detector ring, s is the effective source size, and b is the magnitude of the crystal block effect. The 1.25 factor multiplying the equation is responsible for the reconstruction algorithm used for image formation.

CHAPTER 3

Positron Emission Mammography System

As discussed in the introduction, positron emission mammography, referred as PEM, has been introduced in many research centers around the world [21]-[23], [41]-[44]. The development of PEM was propelled after positive findings obtained with whole-body PET scanners for the detection and the staging of malignant breast tumors and auxiliary nodes involvement. Unfortunately the clinical application of PET is currently restricted by its limited sensitivity in detecting small breast carcinomas and its cost. There was clearly a need for the development of an inexpensive, small, high resolution and high sensitivity PEM device.

We have built a PEM scanner (PEM-1) which produces metabolic images of breasts co-registered with a conventional mammography unit [24, 33].

3.1 Detectors

PEM-1 one consist of two movable planar detectors facing each other. The two detectors can compress the breast by moving up and down. The device was made easily compatible with a conventional X-ray mammography unit for a co-registration. As shown in Figure 3.1 one detector fits between the X-ray tube and the upper compression plate, the second one fits inside the magnification cone which is used in magnification mammography. The purpose of that setting is to obtain the images from

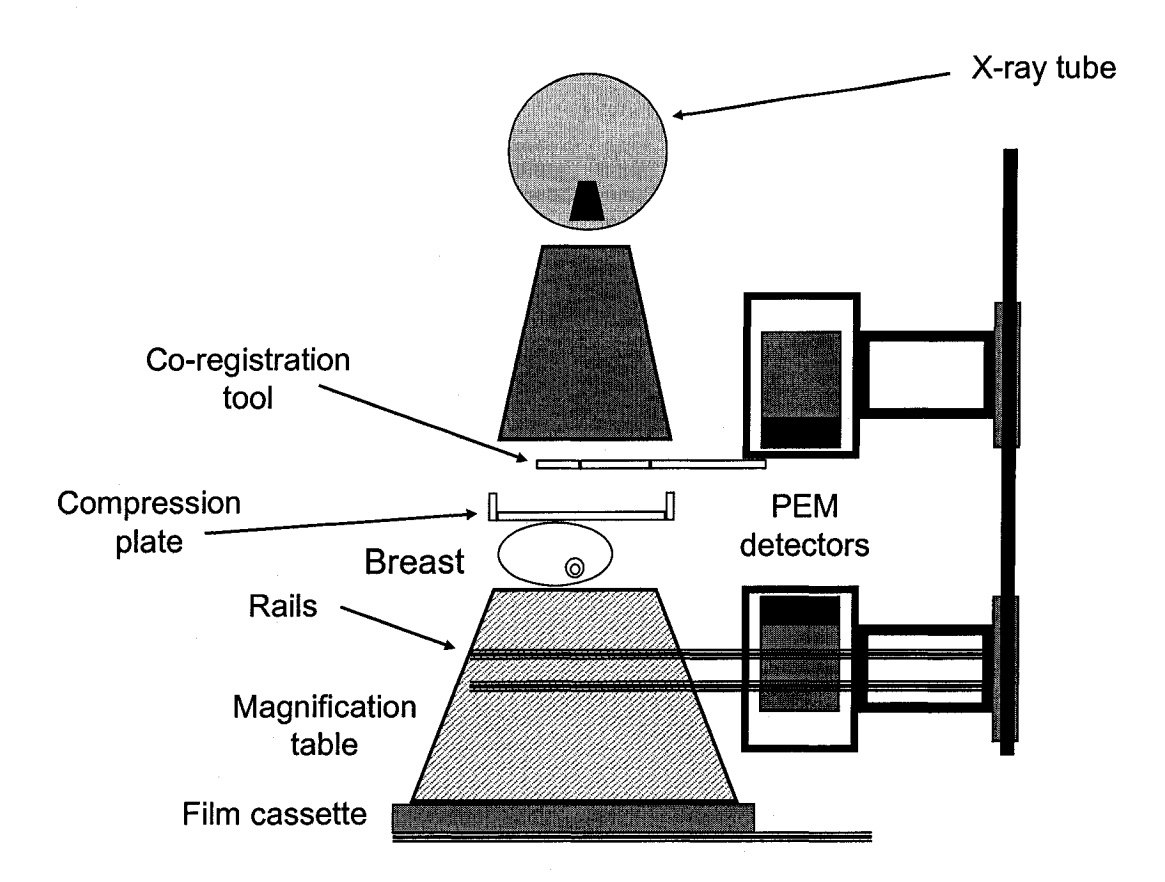


Figure 3.1 Illustration of the PEM-1 scanner fitting into a conventional X-ray mammography unit.

the two modalities with no breast displacement between the two acquisitions. A coregistration tool is used to mark the X-ray film of a square indicating the field of view of the PEM. The co-registration provides accurate localization and helps the physician in his decision making process. The physician can go back and forward looking at the two images and take an optimal decision based on his knowledge in X-ray imaging and PET imaging.

3.2 Crystals and PMTs

Each of the two detector of the PEM-1 system is comprised of an array of four bismuth germanate (BGO) crystal blocks coupled with one position sensitive-photomultiplier tube (PS-PMT). The PS-PMT acts exactly like the four PMTs scheme

used in PET. The PS-PMT output is four analog signals that are digitized and that corresponds to the X+, X-, Y+, and Y- used to positioned the interaction of the event using Anger logic.

Figure 3.2 shows a picture of one crystal block. The crystal blocks are 36 mm x 36 mm x 20 mm and they were cut into a grid pattern using a multiple blade diamond saw. The crystals get cut from the top into a matrix of 18 x 18 crystal elements and 17 x 17 crystal elements from the bottom. The cuts on the top are offset form those on the top by 1.0 mm [24], and the depths of the cuts ensure that an equal number of gamma ray interactions occur in both layers. The light is channelled into

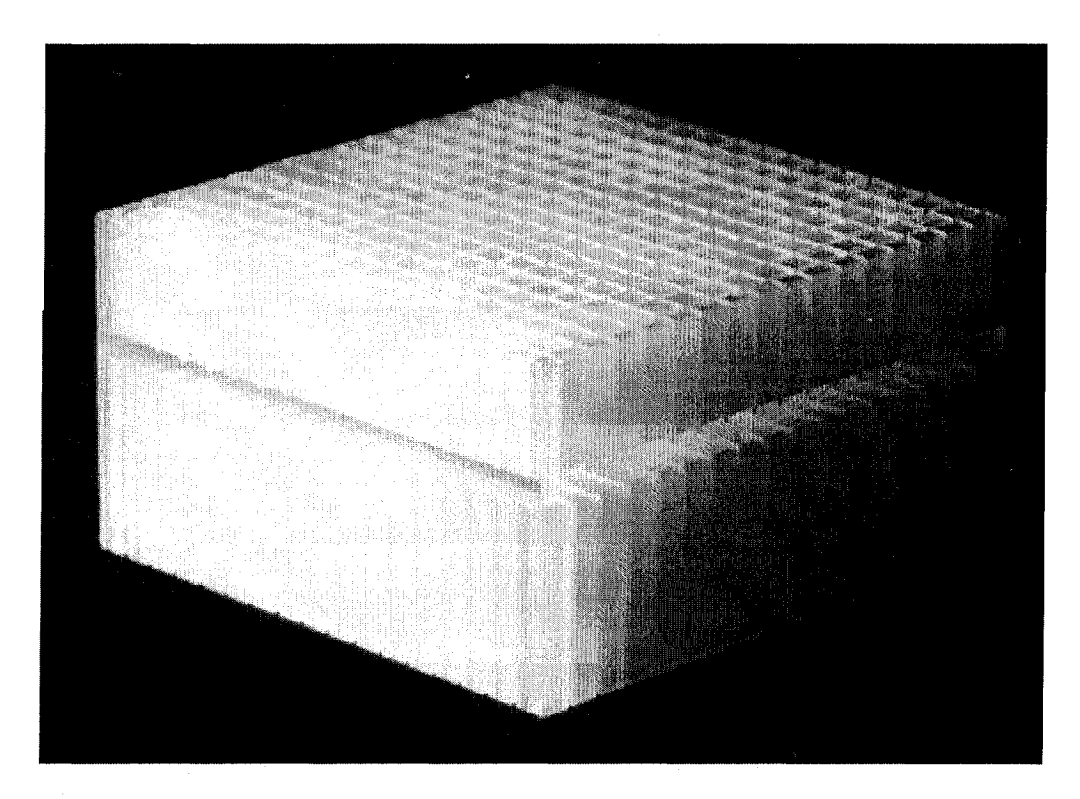


Figure 3.2 Crystal block used in the PEM-1 scanner from Robar et al. [24]. The block is cut on both faces and provides DOI information.

the crystal elements by filling the gaps created by the finite 0.15 mm size of the blade with white opaque light reflecting material. The crystal also is left with an uncut spacing of 2 mm in between the top and the bottom layer to allow the light to travel from one layer to the other. This unique crystal cutting technique provides one bit of information on the depth of the interaction (DOI) also providing a sampling interval of 1.0 mm even though the crystal elements are almost twice that width.

Figure 3.3 illustrates how the DOI information is obtained. A gamma ray photon interaction with the top layer (star labelled 1 in Figure 3.3) will produce

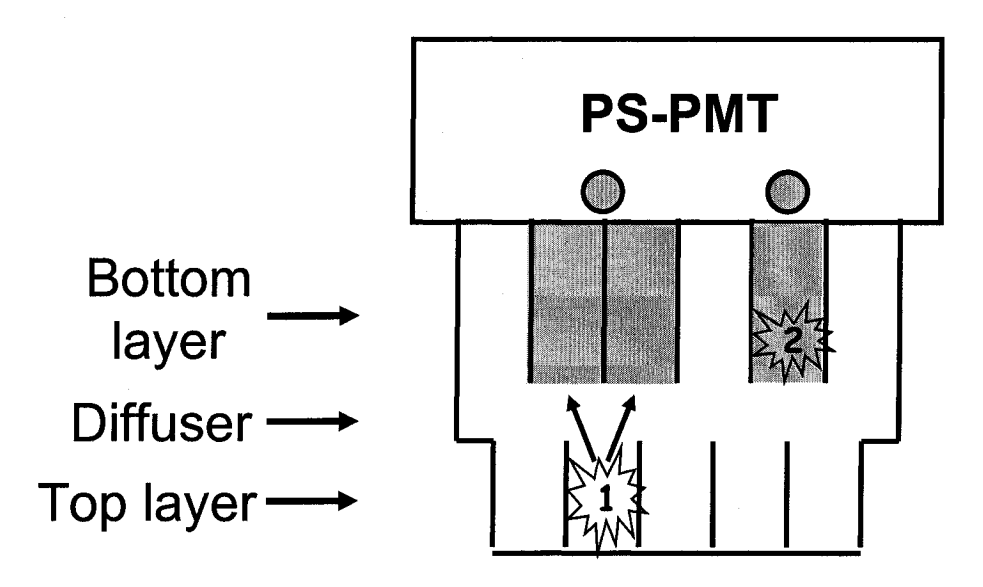


Figure 3.3 Illustration showing how the DOI is obtained. Two gamma ray interactions (the stars); one of which is with the top layer and the other one with the bottom layer.

scintillation light photons in the crystal element of the top layer that will spread into a few crystal elements of the bottom layer. The interaction will therefore appear to come from the center of one of the bottom layer crystal element. Whereas a gamma ray photon interacting directly with the bottom layer (star number 2 in Figure 3.3) will

have its scintillation photons concentrated into the bottom layer and the interaction will appear to come from the middle of one of the crystal element of the bottom layer.

In a more recent study by Zhang et al. [25] it was shown that the removal of the 2 mm uncut spacing between the two layers of the crystal improved the crystal identification. Figure 3.4, taken from Zhang et al., shows the comparison of two crystal identification matrices with and without the uncut spacing. Before the uncut region was removed (Figure 3.4 (a)), the crystal identification matrix has a significant near-far element overlap. After eliminating the spacing (Figure 3.4 (b)), all of the crystal elements can be identify without difficulty. The next generation PEM-2 detectors will not have the 2 mm uncut region and are expected to have a better spatial resolution.

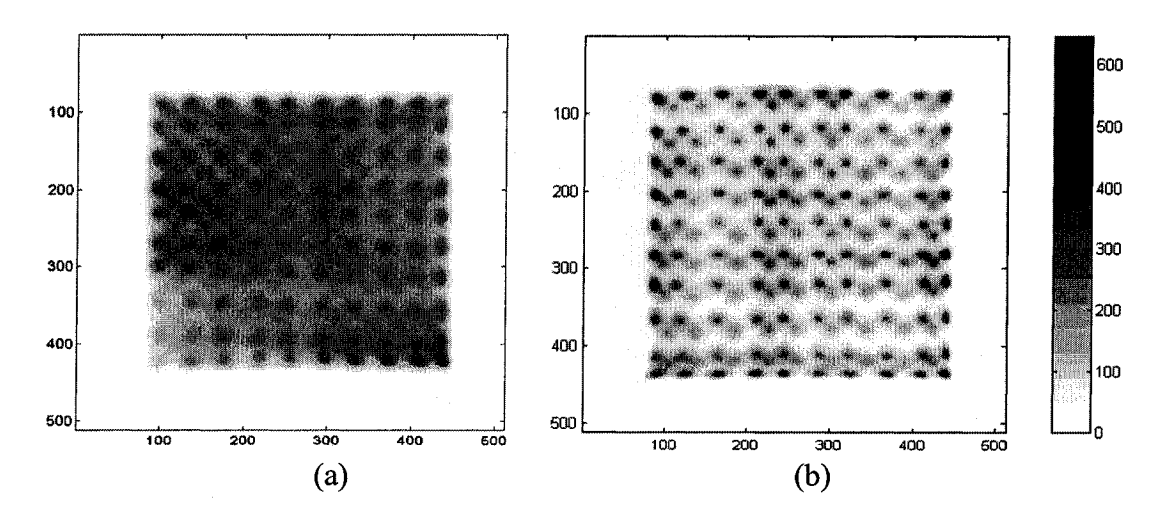


Figure 3.4 Two crystal identification matrices, from Zhang et al. [25], of a BGO crystal block of 10 x 10 and 9 x 9 crystal elements for the bottom and the top layer, respectively. In (a) the crystal was imaged before removing the uncut region and in (b) the uncut region was removed.

3.3 Data Acquisition and Image Formation

When two events occur in coincidence, four signals from each PS-PMT (X+, X-, Y+, and Y-) are digitized with an analog-to-digital converter (ADC) and sent to the computer. Using Equation 2.7, 2.8, and 2.9 the position and the energy of each event is calculated. The first step of the software is to identify the X and Y coordinates of both rays as being associated with a unique crystal element in the top or the bottom layer of the crystal. It does this using the crystal identification matrix. This step, as previously discussed, corrects for spatial non-uniformity of the PMTs. If the energy is above a certain threshold, the count is valid and a LOR connecting the two detectors is back projected across seven equally spaced image planes each of which is a matrix of 128 x 128 integers (32 bits). This type of image formation is referred as a focal plane imaging. An illustration of the focal plane image formation is shown in Figure 3.5. A small source or a tumor positioned in between the two detectors will be well focused in one image plane which is the image plane number three, and will be out of focus in the other planes, providing a three dimensional localization of the tumor. Since the same number of LORs cross each plane, the tumor will appear brighter in the focused plane as shown in Figure 3.5.

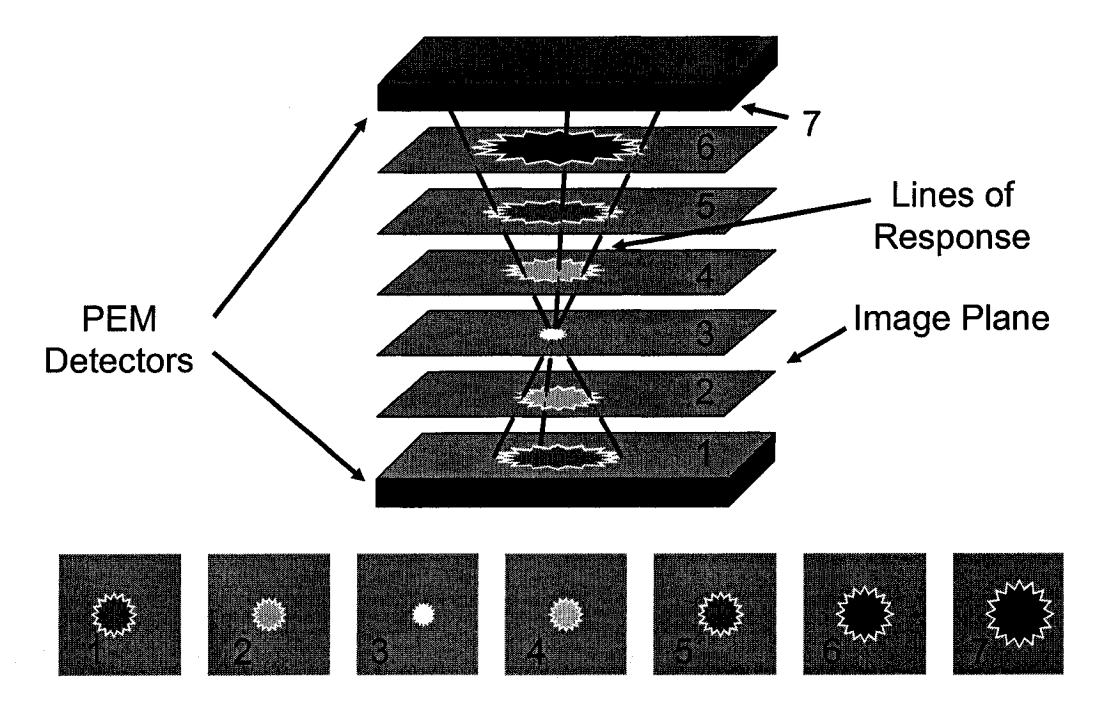


Figure 3.5 Illustration of the focal plane image formation.

When the LOR crosses one plane, the image pixel at that position is incremented according to three factors:

- 1. Each crystal element's relative efficiency.
- 2. The attenuation factor along the LOR.
- 3. A weighting factor which is the reciprocal of the detection efficiency of the detection probability of an event at that location in that plane being detected (that factor is further discussed in Chapter 4).

The benefit of focal plane imaging is that it can be performed in a live fashion. During acquisition, the images are updated each time the input memory buffer fills up. That gives the user the possibility to see how the image changes with time. It also gives the possibility to change the position of the detectors if no hot-spot is seen in the images after a few seconds.

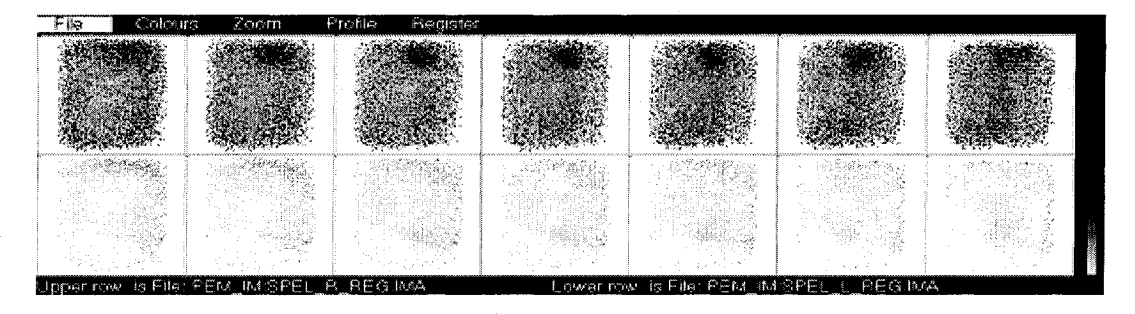


Figure 3.6 PEM display of a true positive patient.

3.4 Image Display

The images are displayed on a color display set up as 14 128 x 128 matrices, seven images across and two down the screen. Figure 3.6 shows the images of a patient with a suspected breast cancer. The suspected breast (right breast) is showed in the top row of images, and the bottom row shows the contralateral breast (left breast). The chest wall of the patient is located on top of the images. The tumor in the top row depicts the focal plane effect, it is mostly focused in the third and fourth images from the left and is diffuse or out of focus in the other images.

The image display software has a few options for image analysis which are all available anytime during and after the acquisition. The image contrast can be adjusted with a simple right click of the mouse, moving in the right and left directions changes the color window width and moving up and down moves the center of the color window width up and down. The software allows one to zoom on one specific image and draw up to four profiles across the same or different images. The user can finally use a display option to overlay the image of the digitized X-ray mammography film

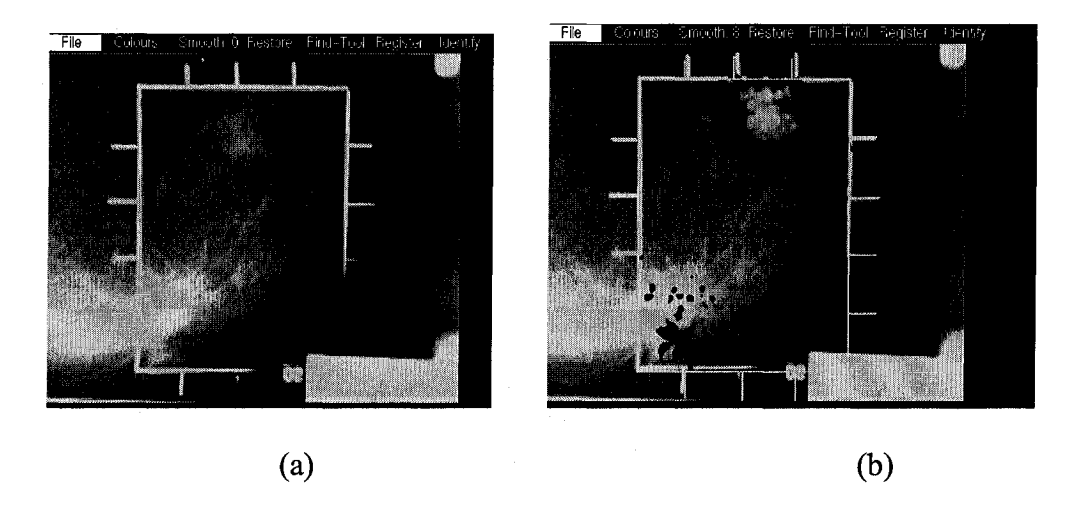


Figure 3.7 PEM co-registration image display. Display of the X-ray mammograph image (a) and overlaid of the X-ray mammograph and the PEM images (b).

and the PEM image as shown in Figure 3.7. The co-registration tool marks the X-ray film with a rectangle visible in Figure 3.7 (a) and is used to align and display the PEM image with the X-ray film. In Figure 3.7 (b), only the PEM image pixels above a certain threshold are displayed in color over the greyscale X-ray mammograph. The threshold can be changed by the user.

CHAPTER 4

Under-Sampling Artifacts

As previously mentioned, a weighted back-projection reconstruction technique is used to reconstruct the images of our PEM-I system. Sampling artifacts are present in the images since the LORs are assumed to start and end on a unique point, the centroid of interaction which is identified as the most probable point of interaction of gamma rays within the crystal element [45]. This effect limits the sampling of the image space and introduces sampling artifacts.

4.1 Determination of the Centroid of Interaction

The identification of the crystal element into which the gamma ray interaction occurred is done using the raw position received by the PS-PMT and the crystal identification matrix. Once the crystal elements are identified for both gamma rays, the reconstruction is done by back-projecting a line of from one detector to the other. The LOR angle with the detectors will be determined with the total distance separating the two crystal elements. Intuitively one would take the distance separating the crystal element with the middle image plane as being the sum of half the thickness of the compressed breast, the thickness of the housing into which resides the detector, and half of the crystal element depth. However the most probable point of interaction of a gamma ray with a crystal element or the centroid of interaction is not exactly at the center of the crystal. A Monte Carlo simulation is required to find the centroid of

interaction. The MNI Monte Carlo Simulation program PETSIM [46] was used to determine the centroid of interaction of the crystal element of both layers in the block. For simplicity, only one value is used for all crystal elements of the same layer. This is slightly incorrect since the penetration angle of the gamma ray with crystal elements located at the periphery of the crystal block will have on average a value smaller than 90 degrees shifting the centroid closer to the patient.

4.2 Sampling Artifacts

Since PEM detectors are planar and stationary, joining the LORs from centroids of interaction causes significant changes in efficiency from one image pixel to the next. Some image pixels will have more LORs crossing them than others. This will create sampling artifacts resulting in a grid like pattern in the images. Of course, the sampling artifact increases the further the image plane is from the middle of the two detectors.

In PET, even if image reconstruction is also performed using back-projection techniques where LORs are drawn between two crystal elements, sampling artifacts are not present since the angular coverage of the detectors is 360 degrees. The LORs are coming from almost all possible angles and a very low amplitude sampling artifact is visible near the edges of the field of view.

A study was performed to compare the imaging performance of a rectangular geometry and a parallel dual-planar geometry PEM scanner [47]. Their rectangular

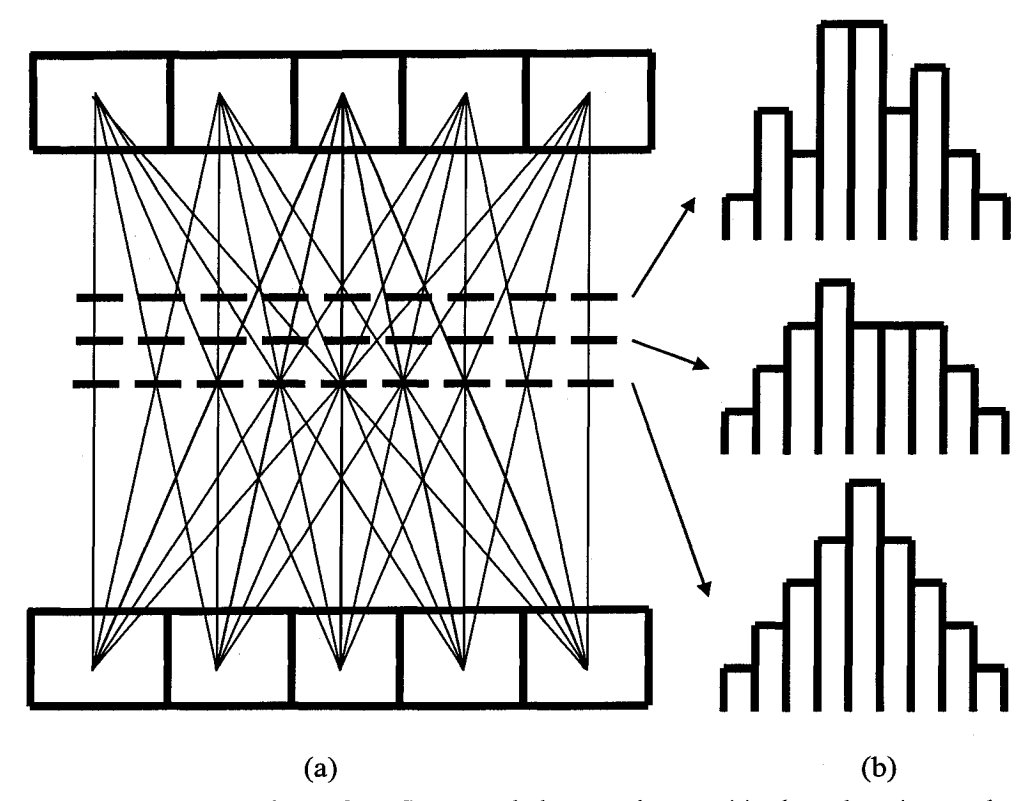


Figure 4.1 2D LORs drawn for a five crystal elements detector (a) where three image planes of nine image pixels are represented by dotted lines. The image pixels are in reality touching each other. The LOR density for the three image plane (b) is calculated by adding the number of LORs that intersect each image pixel.

design consists of four detectors positioned in a rectangle where each detector is placed in coincidence with the other three. As expected, they concluded that the rectangular design performed better than the planar design from the greater angular coverage. The rectangular design is however more complicated to built, would make the price of a scanner go up by a factor of two, and is not easily compatible with an X-ray mammography unit like PEM-1.

The sampling artifacts are presented in Figure 4.1. Figure 4.1 (a) is a simple 2D representation of a five crystal PEM detector. The LORs and three image planes of nine image pixels are shown in Figure 4.1 (a). The LOR density for the three image

planes is shown in Figure 4.1 (b) for each image pixel. The LOR density is calculated by counting the number LORs that intersect each pixel.

Figure 4.2 is a more general version of Figure 4.1. Figure 4.2 is a three dimensional representation of the LOR density through four of the seven image planes. This is a simulation performed with Matlab, The Matworks, Inc. and the code (m-file) is shown in Appendix 1. This simulation was done considering two planar detectors of one layer of 10 x 10 crystal elements each. These histograms are obtained by backprojecting all the possible LORs between the two detectors onto seven image planes from and to the centre of each crystal elements. Each 20 x 20 image planes are incremented by one whenever a LOR crosses an image pixel. From symmetry, only four of the seven image planes are shown in Figure 4.2. The middle plane is shown is Figure 4.2 (a), and the other 3 planes closer to one detector are shown in (b), (c), and (d). The sampling artifact is absent from the middle plane but becomes more of a problem for other planes closer to one detector. Of course the sampling artifact in our PEM-1 system is never as pronounced as shown in Figure 4.2 (d). The reason is that we have not only one but two layers of crystal elements in each detector in our PEM-1 system where all the crystal elements are in coincidence with each other. This geometry quadruples the number of possible LORs compared with a single layer crystal. The simulation was performed with a one layer crystal for demonstration purposes.

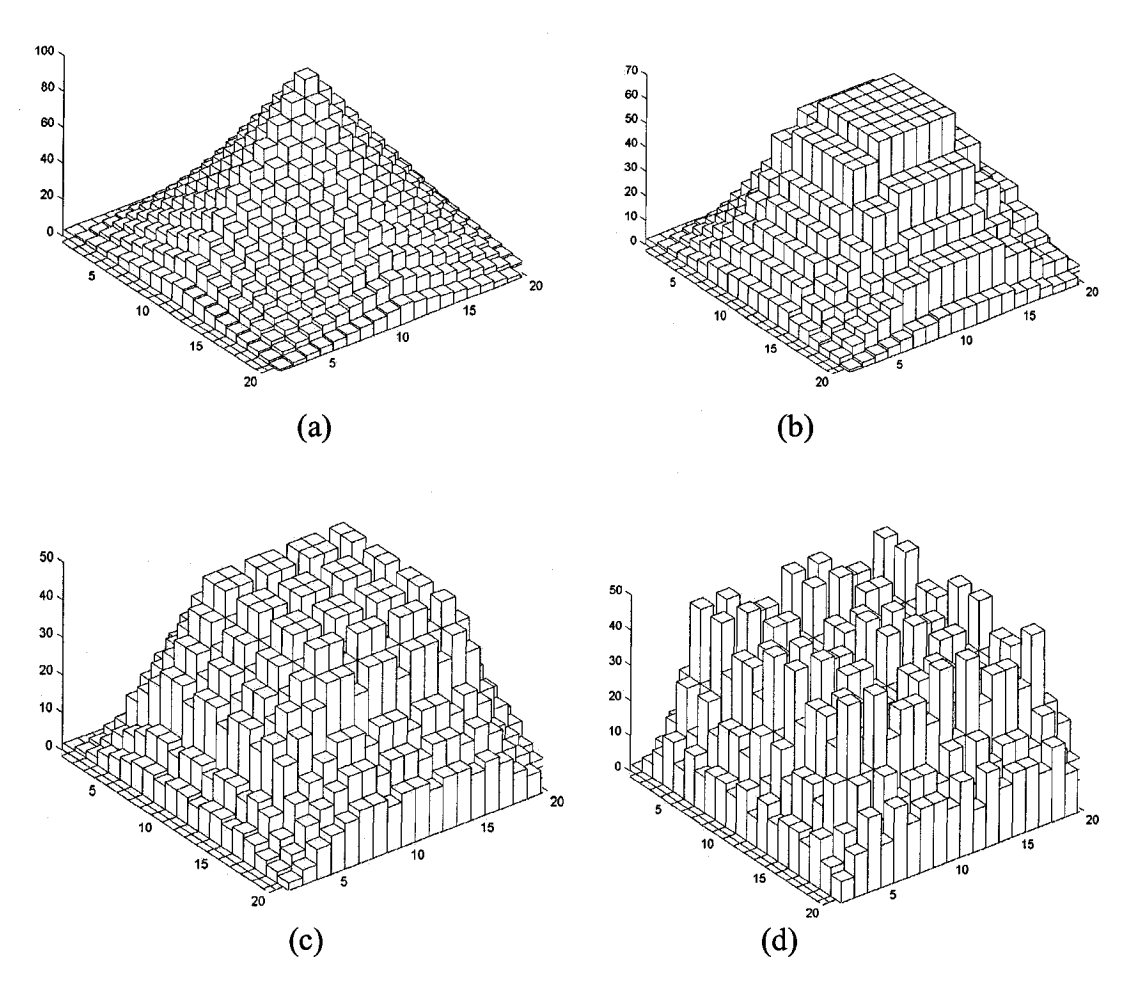


Figure 4.2 Three dimensional histogram of the LOR density through four of the seven image planes. (a) is the middle plane, (b) is the second plane, (c) the third, and (d) is the fourth plane closest to one detector.

4.3 Energy Deposition in the Crystal

A 511 keV gamma ray incident on a crystal will transfer its energy through two main interactions as discussed in Chapter 1. If the interaction is through the photoelectric effect, then all the energy is deposited in one crystal element and the scintillation light will clearly identify that particular crystal element on the face of the PS-PMT. However a 511 keV photon interacting with BGO has approximately a 45 % probability of undergoing a photoelectric interaction [48]. So if the first interaction is through Compton scattering, which is more probable, the photon will deposit some of its energy in the first crystal element it interacts with and the scattered gamma ray may make further interactions in the same or other crystal elements. Even for a 180 degree scatter the scattered photon has more energy than the recoil electron. If the scattered gamma ray is absorbed by an adjacent crystal element, the scintillation light will be distributed in two crystal elements, while the amount of scintillation photons received at the PS-PMT surface will be equivalent to a 511 keV photon. Hence, the event will be accepted but position given by the PS-PMT will be erroneous, it will correspond to a crystal element located somewhere in between the two interactions.

4.4 Sub-Crystal Identification

The problem of energy deposition through multiple interactions is especially present in PEM scanners since the crystal block is very finely pixilated. Each crystal elements of the two layers is 1.9 mm x 1.9 mm, which produces a crystal center-to-center separation of 1.4 mm on the diagonal of the block. This will have the effect of overlapping neighbouring ROIs in the crystal identification matrix. From what was

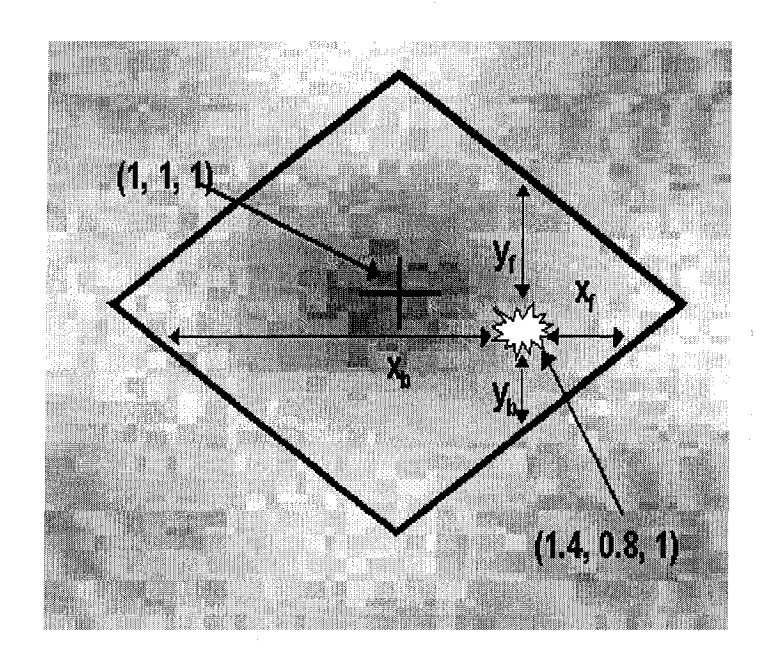


Figure 4.3 ROI for crystal element (1, 1, 1). The sub-crystal identification (1.4, 0.8, 1) is calculated using the relative position of the event to the boundary of the ROI.

discuss in the last section, the further away the point of interaction is from the center of the ROI, the more likely it is to be in the next crystal element. The "sub-crystal identification" consists of putting the event closer to the next most probable crystal element. Figure 4.3 shows how the sub-crystal identification is performed. For simplicity, LORs were not allowed to shift between crystal layers, i.e. in the z direction. If the most probable crystal element is x (1 in Figure 4.3), then the sub-crystal position is determined from the relative distance of the event from the boundary of the ROI in the crystal identification matrix. The final position X (1.4 in Figure 4.3) is defined as:

$$X = x + \frac{x_b - x_f}{2 \cdot (x_f + x_b)} \tag{4.1}$$

where x_f is the distance, in pixel, forward to the boundary of the ROI and x_b is the distance, in pixel, backward to the boundary of the ROI. Because of the 2 in Equation 4.1, the final position runs from x - 0.5 to x + 0.5. Similarly the final position Y (0.8 in Figure 4.3) is defined as:

$$Y = y + \frac{y_b - y_f}{2 \cdot (y_f + y_b)} \tag{4.2}$$

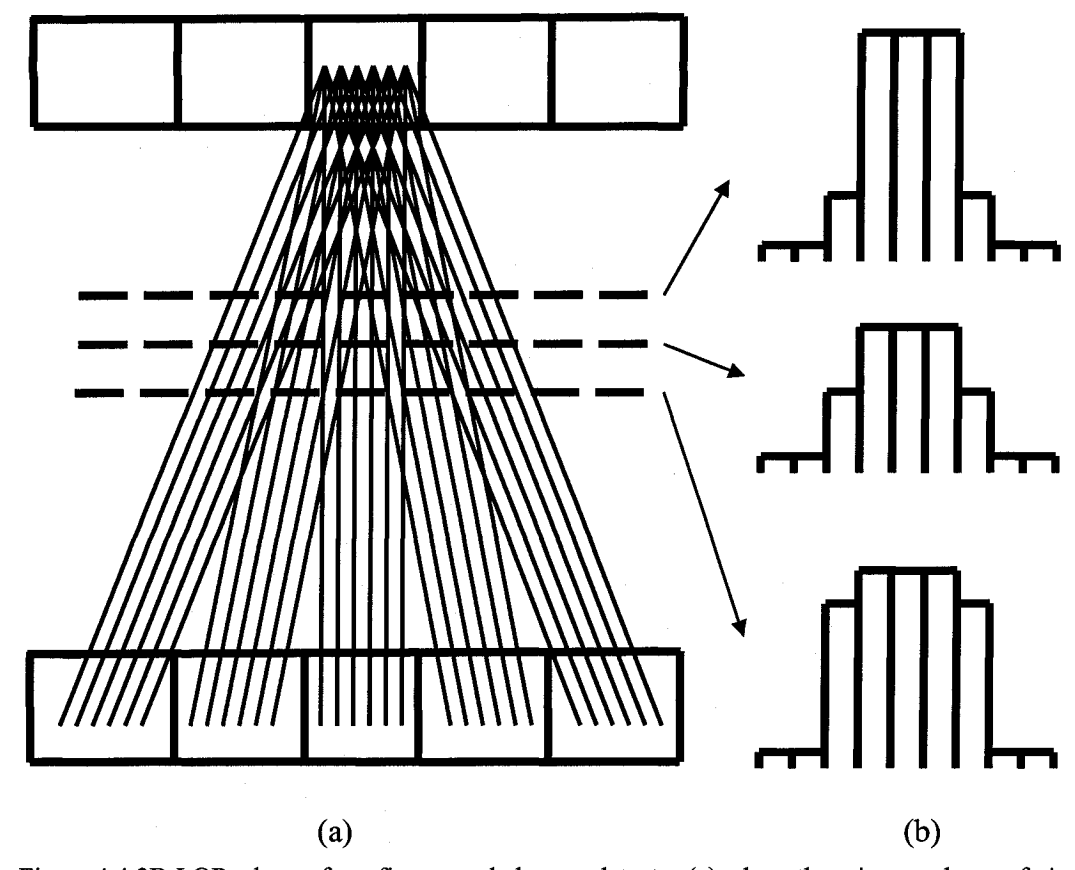


Figure 4.4 2D LORs drawn for a five crystal element detector (a) where three image planes of nine image pixels each are represented by dotted lines. The image pixels are in reality touching each other. The LORs are shown for only one crystal element using sub-crystal identification .The LOR density for the three planes is (b) calculated by adding the number of LORs that intersect each image pixel.

where y_f is the distance forward to the boundary of the ROI and y_b is the distance backward to the boundary of the ROI. A demonstration of the LORs pattern and LOR density of three image planes using sub-crystal identification for one crystal element is shown in Figure 4.4 (a) and (b), respectively.

Figure 4.5 is a three dimensional representation of the LOR density through four of the seven image planes obtained using a sub-crystal identification. The simulation was exactly like in Figure 4.5 but the number of LORs was increase. Instead of having only one possible point for the LOR start and end points similar to

the centroid, we used four different points within each crystal elements. As before, all the possible LORs were backprojected and the image matrix was incremented each time a LOR crossed it. The improvement in sampling density from Figure 4.2 is remarkable. Now the planes located close to one detector are free of sampling artefacts. Of course the distribution is not flat throughout the field of view and that is from the fact that the probability for detection is higher in the middle of the field of view than on the periphery. That is further discussed in the next chapter.

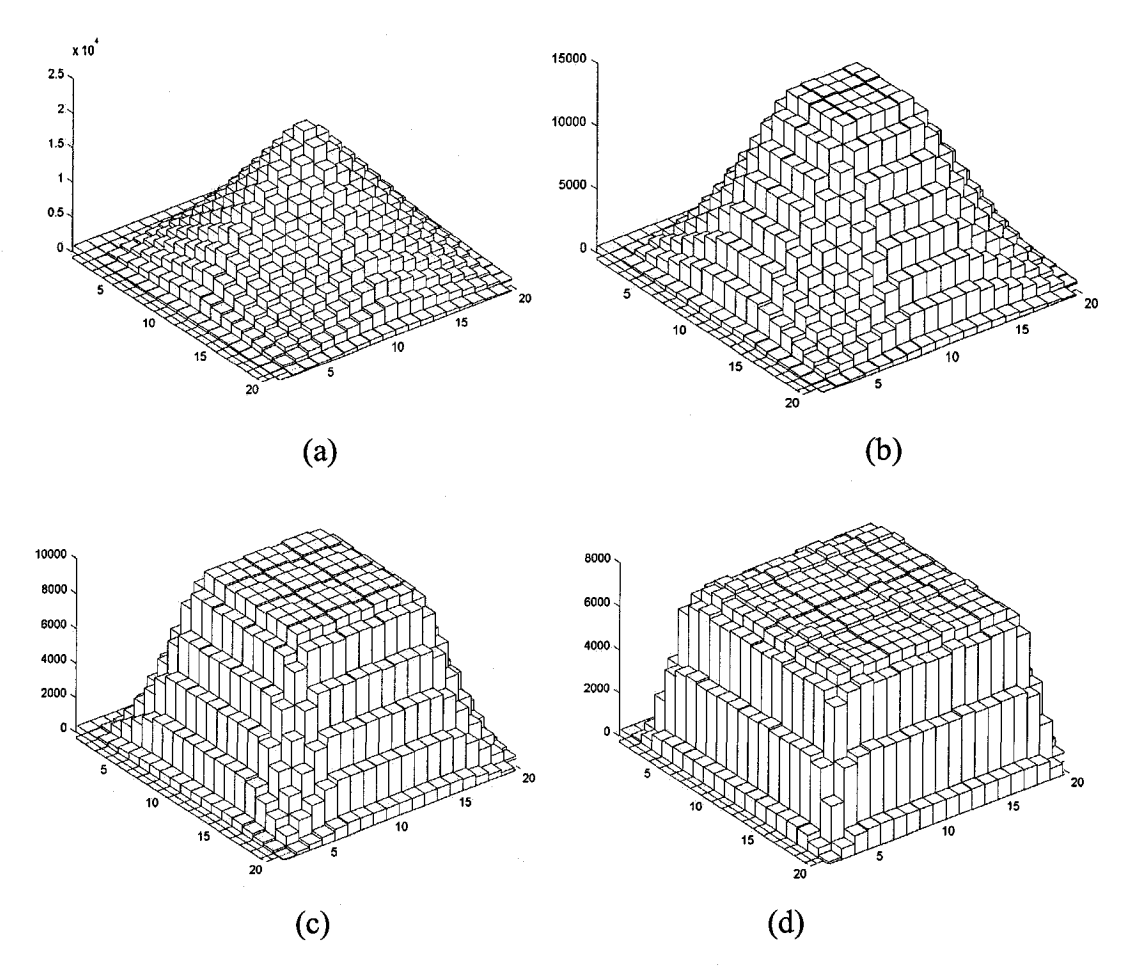


Figure 4.5 Three dimensional histogram of the LOR density through four of the seven image planes. (a) is the middle plane, (b) is the second plane, (c) the third, and (d) is the fourth plane closest to one detector.

CHAPTER 5

Solid Angle Function

During the focal plane image reconstruction, the value by which an image matrix element is incremented, I, is weighted by several factors according to,

$$I = K \frac{e^{\mu l}}{W(x, y, z)\varepsilon_A \varepsilon_B}$$
 (5.1)

where ϵ_A and ϵ_B are the efficiencies of the crystal elements of detectors A and B respectively, in which the gamma rays were absorbed. W(x ,y ,z) is a weighting factor also called the "solid angle function" that accounts for the dependence of the detection probability of an annihilation pair at the (x,y,z) location in between the two detectors. μ is the linear attenuation coefficient of the breast tissue, and 1 is the path length along the LOR through the breast and the compression plate. Finally, K is a factor required to scale so that it is in the appropriate range (0 to 100) to update an integer image matrix.

The weighting factor guarantees that a uniform activity concentration produces a uniform image in the seven image planes, event though the efficiency or detection probability is much greater in the center of the detector than in the periphery of the field of view.

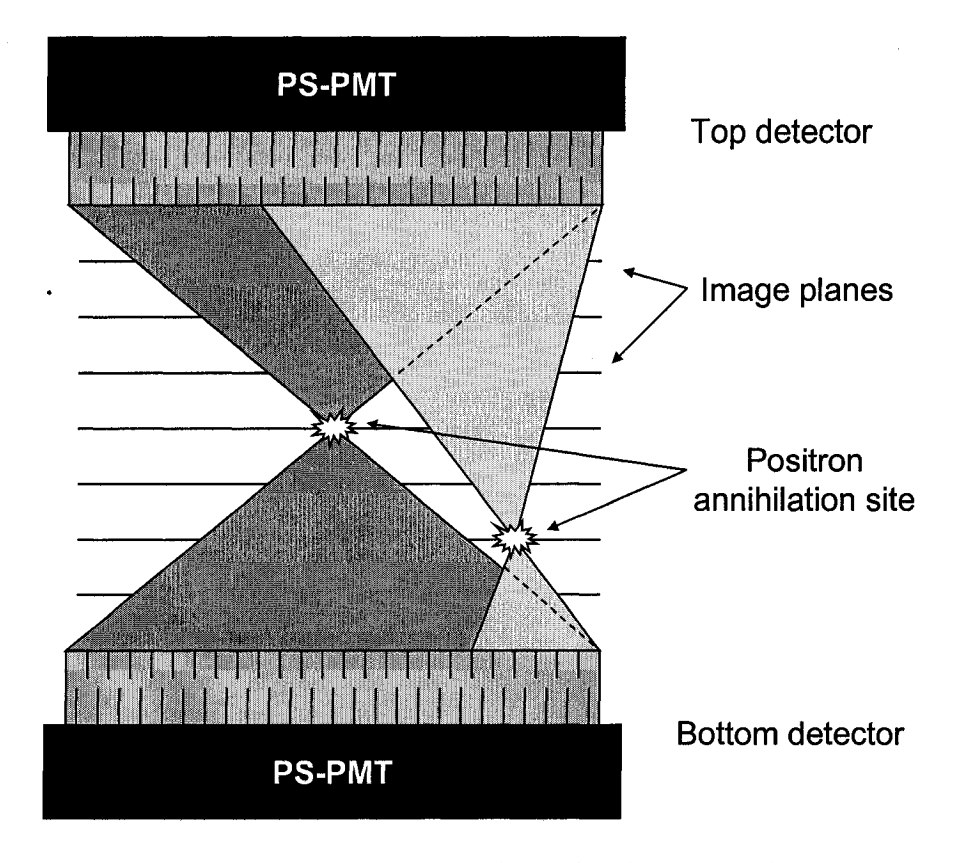


Figure 5.1 Two dimensional illustration of the solid angle subtended by the two different annihilation sites.

5.1 Detection Probability

Since we are detecting two gamma rays emitted from the positron annihilation at 180 degrees from each other, the detection probability of an event is strongly dependent on the positron's site of annihilation. The detection probability will be proportional to the solid angle subtended by the positron annihilation site with the two detectors. Figure 5.1 shows a two dimensional illustration of the solid angle subtended by two annihilation sites. The position dependence on detection probability is clearly shown; the positron annihilation site located in the middle of the field of view will be

detected with a much higher efficiency than the one located away from the middle of the field of view.

The detection probability was first calculated analytically by Yani Picard [26]. Let the dimensions of the detectors be 2X by 2Y and separated by 2Z. The positron annihilation is at x, y, z and produces two gamma rays which make an angle α with the z axis projected on the x, z plane, and β with the z axis projected on the y, z plane. The detection probability, DP(x,y,z,X,Y,Z) of detecting an event at x, y, z is given by;

$$DP(x, y, z, X, Y, Z) = \frac{1}{2\pi} \int_{\alpha_i}^{\alpha_f \beta_f} \int_{\beta_i}^{e^{\left(-\frac{\mu_{water}D}{\cos\alpha\cos\beta}\right)}} \left(1 - e^{\left(-\frac{\mu_{BGO}T}{\cos\alpha\cos\beta}\right)}\right)^2 d\Omega$$
 (5.2)

where T is the thickness of the crystal, D is the thickness of the compress breast section, and α_i , α_f , β_i , and β_f are defined as:

$$\alpha_i = -\tan^{-1} \left(\frac{X - |x|}{Z - |z|} \right) \tag{5.3}$$

$$\alpha_{f} = \frac{\tan^{-1}\left(\frac{X - |x|}{Z - |z|}\right) \rightarrow \left|\frac{z}{x}\right| \left\langle \frac{Z}{X}\right|}{\tan^{-1}\left(\frac{X + |x|}{Z + |z|}\right) \rightarrow otherwise}$$
(5.4)

$$\beta_i = -\tan^{-1} \left(\frac{Y - |y|}{Z - |z|} \right) \tag{5.5}$$

$$\beta_{f} = \frac{\tan^{-1}\left(\frac{Y - |y|}{Z - |z|}\right) \to \left|\frac{z}{y}\right| \langle \frac{Z}{Y}}{\tan^{-1}\left(\frac{Y + |y|}{Z + |z|}\right) \to otherwise}$$
(5.6)

The detection probability distribution calculated with Equation 5.2 for the PEM-1 detector with a detector separation of 50 mm for the central plane is pictured in Figure 5.2. As expected, the value of the detection probability is highest in the middle of the detector and decreases smoothly for points away from the center of the field of view.

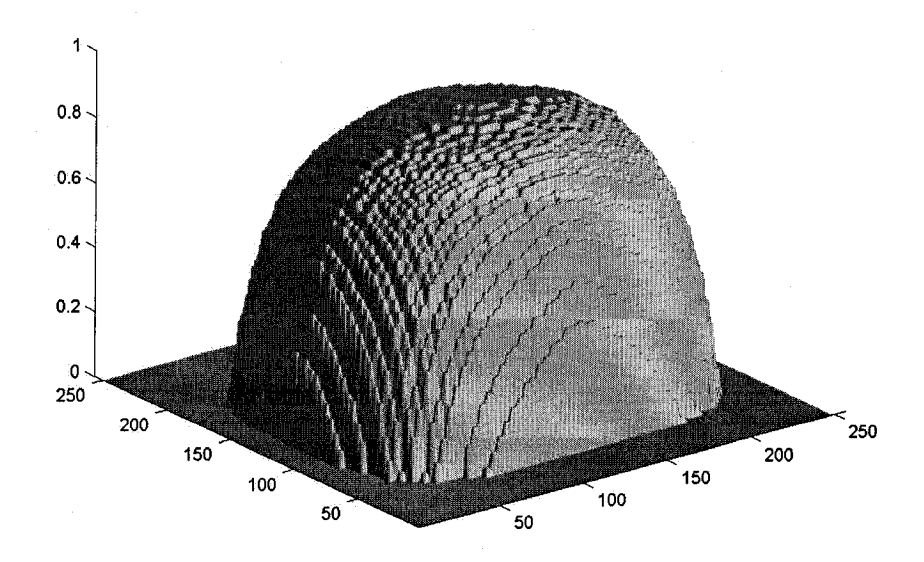


Figure 5.2 Detection probability function or solid angle function for points in a central plane for detector spacing of 50 mm.

5.2 Solid Angle Function

The image is form on seven planes by dividing by the weighting factor equal to the detection probability DP(x, y, z, X, Y, Z) given in Equation 5.2 to the image pixel (x, y) at which the line joining the two coincident crystal elements intersects the image planes. The detection probability is actually independent of the angle of an individual gamma ray pair with respect to the detectors, the only dependence is one the detector separation. The detection probability can thus be tabulated into a LUT for later use during the display. During the construction and calibration of PEM-1, the detection probability were calculated and stored into a LUT called the solid angle function. The solid angle functions were calculated for different detector separations.

Since the solid angle function is only dependent on the detector separation, it can be applied only once all the LORs have been backprojected. The image matrices are hence divided by the solid angle function as the last step in the reconstruction. This process reduces the reconstruction time which is precious for a live display.

5.3 Re-Ordering the Solid Angle Function and the Smoothing Algorithm

As discussed in the previous section, the detection probability is higher for points in the middle of the field of view and lower for point away from the field of view. The number of annihilations detected, or counts detected will be lower in the periphery than in the middle of the field of view. In Poisson counting statistics, the noise is proportional to the square root of the number of counts. Considering this, the signal-to-noise ratio (SNR) is lower in regions where counts are lower. Or, the noise-to-signal ratio (NSR) is higher in the periphery of the image where the number of counts is lower. Since the solid angle function has low values in the peripheral regions of the image; dividing the image where the NSR is high by a small number will amplify the NSR of the final image in those regions.

For example, if we consider 100 counts for an image pixel located in the middle of the central image plane and 10 counts for an image pixel located at the periphery of that same image plane. Poisson statistics dictates that the noise be $\pm (100)^{1/2} = \pm 10$ and $\pm (10)^{1/2} = \pm 3.2$ for the central and the peripheral image pixel respectively. Since the image is supposed to be uniform the solid angle function will

have values of 1 and 1/10 for the central and the peripheral image pixel respectively. Dividing by the solid angle function will make the final image pixels be 100±10 and 100±32 for the central and the peripheral image pixel respectively. Hence the noise and the NSR will be amplified for peripheral image pixels.

The smoothing algorithm is an option available with the PEM-1 display software. The smoothing algorithm helps in improving the image contrast of interesting clinical features like lesions or hotspots in the image. The smoothing algorithm filters the seven images with a 3 x 3 box car smoothing. The 3 x 3 box car smoothing is a simple algorithm that smoothes the images by changing the value of each pixel with the average value of the nine neighbouring pixels.

Before displaying the images they are scaled to the maximum value in the image display. If the image is close to uniform its maximum pixel value will be at the edge due to noise amplitude at the periphery. Hence smoothing the image will increase the dynamical range of the image.

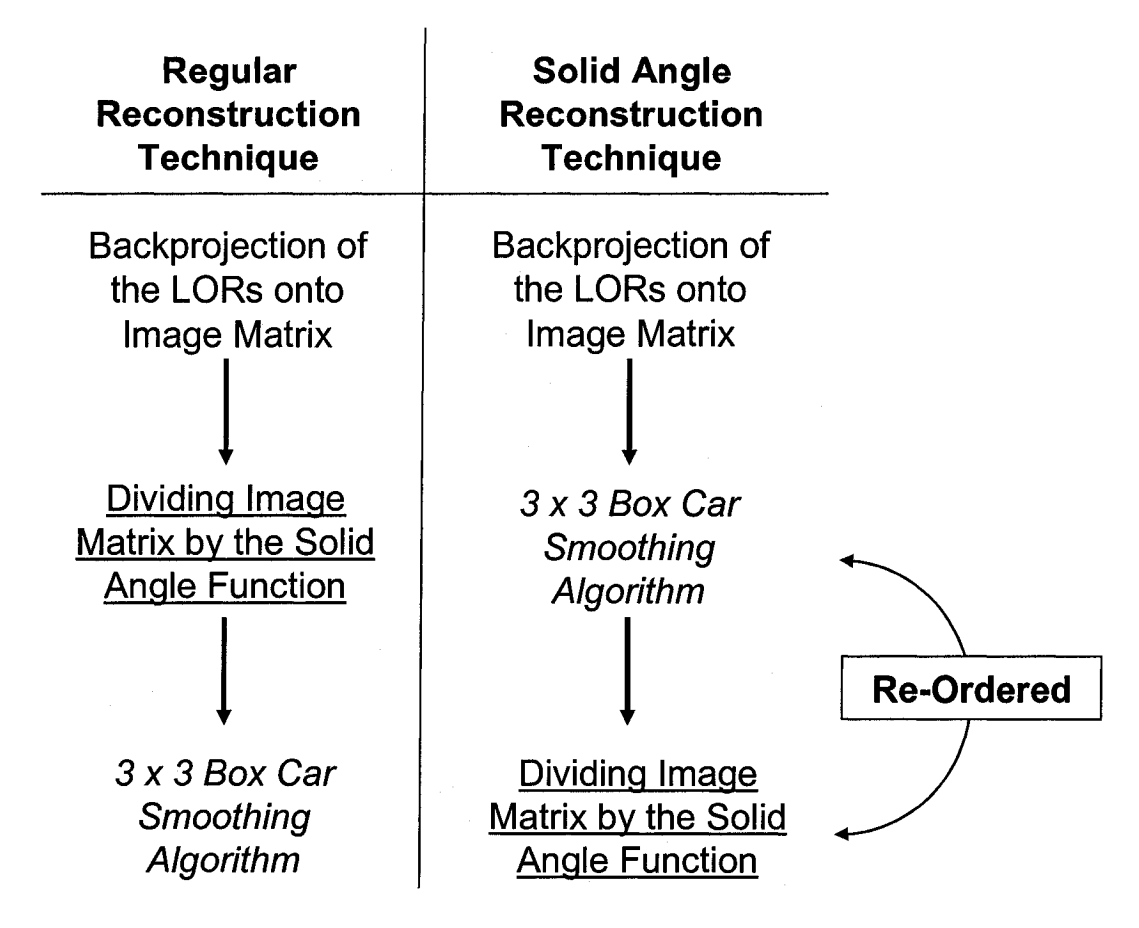


Figure 5.3 Regular and the solid angle reconstruction process.

The "solid angle technique" consists of re-ordering the application of the solid angle function and the smoothing filter. Figure 5.3 is a schematic diagram of the procedure for the regular and the new solid angle reconstruction technique. In the regular reconstruction technique, the LORs are backprojected, the images are divided by the solid angle before getting displayed on the screen, and then the smoothing filter can be applied. In the solid angle technique the two last steps are re-ordered so that the solid angle function divides the already smoothed image. This technique should reduce the NRS amplification and hence the noise amplitude in the peripheral regions of the images.

CHAPTER 6

Quantitative Analysis

To test the performance of the sub-crystal identification technique and the solid angle technique, a quantitative analysis performed on different types of images was performed. The image quality improvement was quantified with respect to SNR, contrast resolution, noise, and spatial resolution. The data, taken from two phantoms studies acquired with the PEM-I detector by former students of the MNI computer lab, was reformatted and re-analyzed using the two new techniques.

The diagnostic improvement was also analyzed using an ROC curve analysis. Patient data from a clinical trial conducted in 1997 at the MNI was used for that analysis.

6.1 Breast Phantom Study

In 1999, a custom breast phantom and a novel technique for fabricating very small wall-less radioactive hot-spots were developed in our lab in order to quantify the emission images. The breast phantom consists of an L-shaped Plexiglas container that is filled with water and FDG to simulate background. The hot-spot was made by adding FDG to a solution of Agarose and was positioned to different position in the container using a needle [49].

Contrast resolution of the detector was quantify using a 20 mm diameter hotspot for a set of different true contrasts C_{TRUE} (i.e. different background and hot-spot activities) which were calculated using:

$$C_{TRUE} = \frac{A_T}{A_R} \tag{6.1}$$

where A_T is the tumor (hot-spot) activity and A_B is the background activity.

The projected contrast is however different than the true contrast. It is defined as the ideal contrast seen by the detectors in a projection image. If the breast is compressed to D cm and the lesion is of radius R, than the projected contrast, C_{PROJ} , will be:

$$C_{PROJ} = C_{TRUE} \cdot \frac{2R}{D - 2R} \tag{6.2}$$

PEM image contrast C_{PEM} was measured by drawing a region of interest (ROI) around the hot-spot in the best focused image. It was calculated using:

$$C_{PEM} = \frac{T}{B} \tag{6.3}$$

where T is the average tumor signal and B the average background signal corresponding to the number of counts inside and outside the ROI, respectively. With the same ROI, signal-to-noise (SNR) was calculated using:

$$SNR = \frac{T}{\sigma_B} \tag{6.4}$$

where σ_B is the standard deviation of the background, i.e. the number of counts in the image outside the ROI.

6.2 Point Source Study

Spatial resolution measurements were done with a ⁶⁸Ge point source (0.78 mm diameter). Four experiments were done with one point source positioned at different distances from one detector (3 cm, 2 cm, 1.5 cm and 1 cm) for a total detector separation of 8 cm. X-axis and Y-axis profiles crossing the peak of the point source were fitted with gaussian curves. The standard deviation and the mean square difference of the fit were used as factors representing resolution and noise, respectively.

6.3 Clinical Trial Study

In 1997, a clinical trial was conducted with 16 women with suspected breast cancer. The patients were scanned 40 to 60 minutes after the injection of 75 MBq of FDG. The suspicious breast was imaged first followed by the other one. Using visual

inspection, PEM images were classified as positive if significant uptake (hot-spot) was seen in the region corresponding to the tumor compared with the uptake in the background, i.e. the region outside the hot-spot. A minimum of 2:1 hot-spot-to-background ratio was required to declare the patient positive. All the clinical trial studies were replayed and verified for any diagnostic improvements.

6.4 ROC Curve Analysis

The ROC curve analysis was conducted to verify any accuracy improvement between the reformatted data and the original data. ROC analysis is a recognized method to access the accuracy of a diagnostic test [50]-[52].

Table 6.1 shows how a diagnostic test result is classified. The ROC curve is obtained by plotting the sensitivity (y-axis) versus 1-specificity (x-axis). The sensitivity is the proportion of patients *with* the disease who test positive and is defined as:

Sensitivity =
$$P(T^+|D^+) = \frac{TP}{TP + FN}$$
 (6.5)

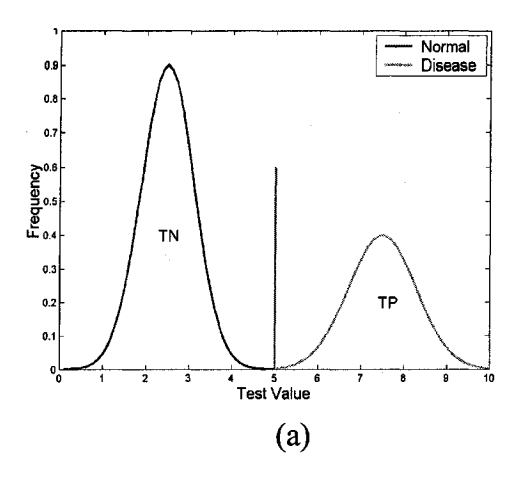
The specificity is the proportion of patients *without* the disease who test negative and is defined as:

Specitivity =
$$P(T^-|D^-) = \frac{TN}{TN + FP}$$
 (6.6)

Table 6.1 Basic diagnostic test interpretation.

	Disease Present	Disease Absent
Test Positive	True Positive (TP)	False Positive (FP)
Test Negative	False Negative (FN)	True Negative (TN)

In order to build an ROC curve, the outcome of a test must be quantified with a diagnostic test value. Figure 6.1 is a graph of the number of patient with and without the disease arranged according to a diagnostic test value. An idealized perfect test is shown in Figure 6.1 (a), for which there is no overlap between normal and disease patients. This test would have 100 % accuracy in distinguishing between patients with and without the disease. A more realistic diagnostic test is shown is Figure 6.1 (b). This distribution overlaps; the test doesn't distinguish normal from disease with 100 % accuracy. In practice, we choose a cut point, indicated by the vertical line, above which we consider the patient positive and below which we consider the patient negative. A low cut point value will have a high sensitivity but a low specificity and a high cut point value will have a high specificity and a low sensitivity. Thus any chosen cut point value is a trade off between sensitivity and specificity.



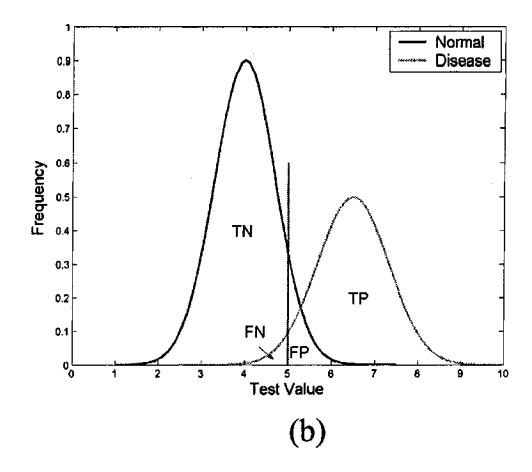


Figure 6.1 Graph of the number of patient with and without the disease arranged according to the value of a diagnostic test. (a) is a perfect test and (b) is an imperfect test.

The ROC curve is obtained by plotting the sensitivity as a function of specificity for different cut point values. A typical ROC curve is shown in Figure 6.2. The diagonal line, called the pure guess line in Figure 6.2 shows the outcome of a purely random test. The closer the ROC curve gets to the left-hand border and then the top border of the ROC space, the more accurate the test. Hence, the area under the curve can be used to verify and compare the accuracy of different diagnostic test.

An ROC curve analysis was performed to verify if the sub-crystal identification and the solid angle techniques could improve the accuracy of PEM-1. For that, six medical physics students were shown 28 images in a random order; 14 left breast and 14 right breast images. Half of them received the original data and the second half received the reformatted data. The reformatted data was processed using both the sub-crystal identification and the solid angle techniques. They were first taught how to use the PEM-I display program and then trained with two real cases, i.e. one true-positive

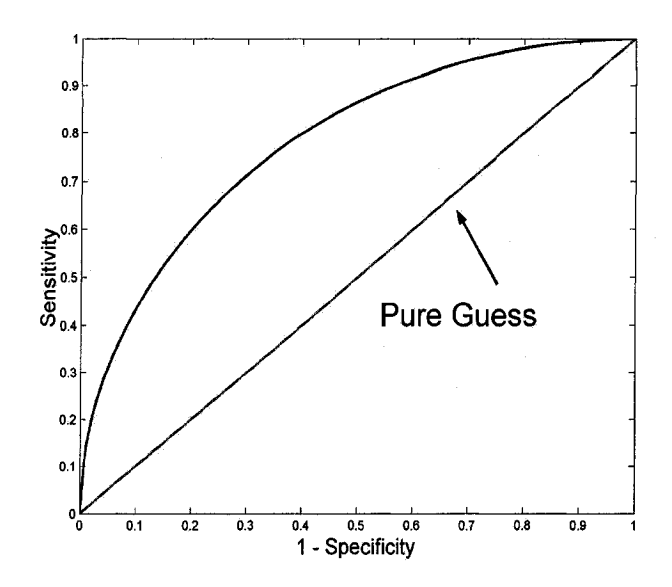


Figure 6.2 Typical ROC curve.

and one true-negative. They were asked to quantify each image according to five diagnostic test values as shown below:

Test Value 5	Tumor definitely present
Test Value 4	Tumor more present than absent
Test Value 3	Tumor equally present and absent
Test Value 2	Tumor more absent than present
Test Value 1	Tumor definitely absent

The sensitivity and specificity were calculated for different cut points. Sets of ROC curves were obtained for each student by plotting the sensitivity against 1-specificity. The data was also put together to form two average ROC curves. The

areas under the ROC curves were used to quantify accuracy of the regular and the new reconstruction method.

Results

7.1 Contrast Phantom Measurements

A comparison of the regular identification technique and the sub-crystal identification technique using a contrast phantom measurement is shown in Figure 7.1. The images generated using the sub-crystal identification technique were obtain by shifting the start and end point of the LORs by an increment as calculated with equation 4.1 and 4.2 for the X and Y position, respectively. Equation 4.1 and 4.2 are given for a continuous re-sampling but of course this was not possible to implement. It was found that using one digit after the point, similar to separation the crystal elements in 10 bins, gave good results; more bins wouldn't improve the image quality. The X-axis and Y-axis profiles through the hot-spot are also shown. For that example, 114 884 counts were acquired, C_{TRUE} was 10, C_{PEM} increased by 5 %, and SNR improved by 10 %. White circles have been overlaid on the images to attract the reader's attention to those regions. One can notice in the circles of Figure 7.1 (a) the pattern reflecting sampling artifacts. The pattern is significantly reduced in Figure 7.1 (b). From those comparisons, one immediately notices a reduction in noise due to the sub-crystal identification.

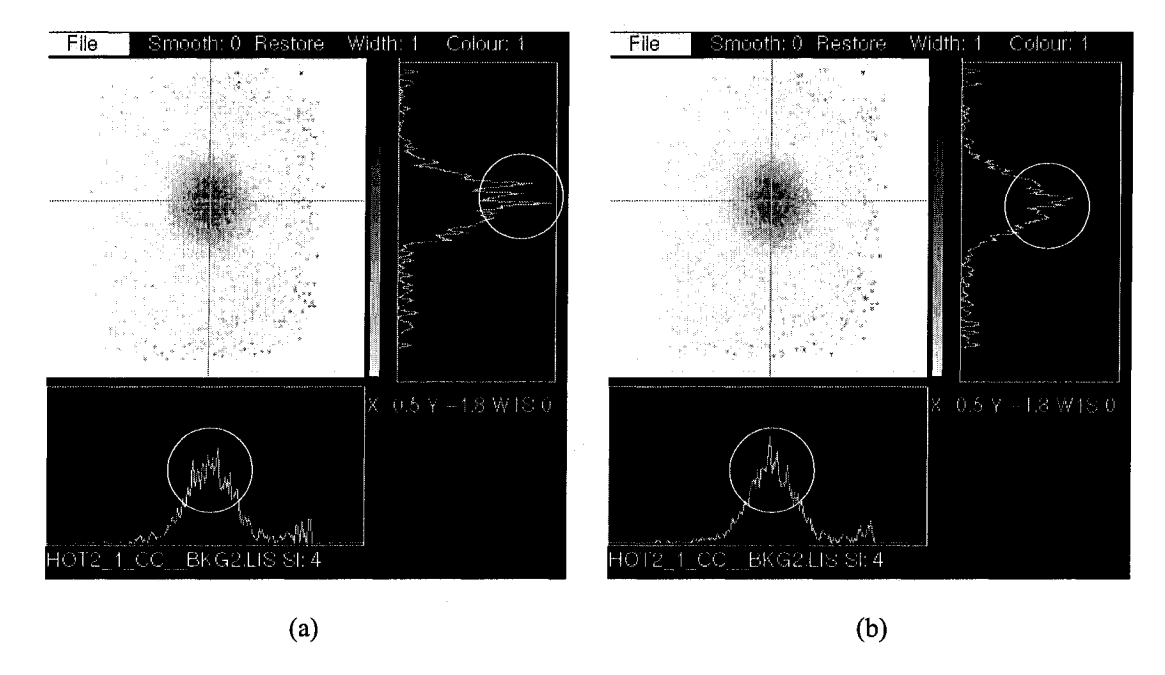


Figure 7.1 Comparison of the regular identification technique (a) and the sub-crystal identification technique (b) of a contrast phantom experiment. The X-axis and Y-axis profiles are shown where the scale is relative to the highest pixel value of the image. The profiles from (a) are replicated in (b) for comparison.

Table 7.1 shows the calculated C_{PEM} and SNR for a range of C_{TRUE} . For all values of C_{TRUE} , both the C_{PEM} and the SNR increased for an average of 3 % and 5 %, respectively.

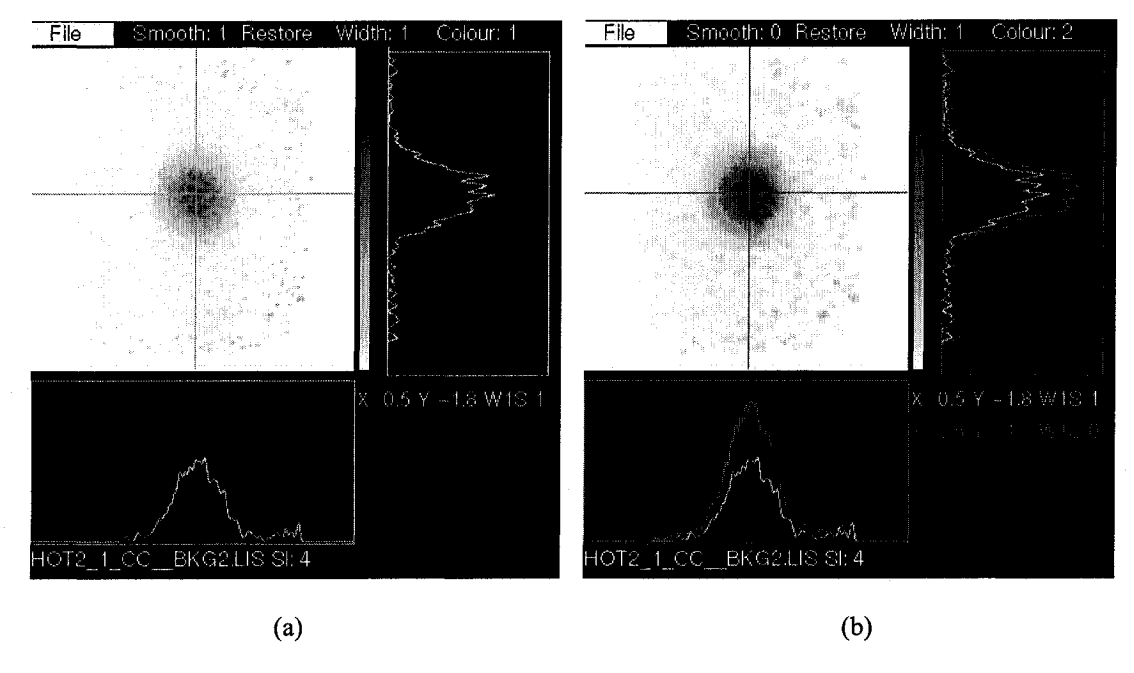


Figure 7.2 Comparison of the regular technique (a) and the solid angle technique (b) of a contrast phantom experiment. The X-axis and Y-axis profiles are shown where the scale is relative to the highest pixel value of the image. The profiles from (a) are replicated in (b) for comparison. The SNR is improved when smoothing the image before the solid angle function.

Table 7.1 PEM contrast and SNR obtained for a set of projected contrast using the regular and the sub-crystal identification.

		Regular Identification		Sub-Crystal Identification	
True Contrast C _{TRUE}	Projected Contrast C _{PROJ}	PEM Contrast C _{PEM}	SNR	PEM Contrast C _{PEM}	SNR
10	5.6	1.67	2.46	1.70	2.65
19	10.5	2.74	3.21	2.83	3.34
47	26.1	4.88	4.30	5.04	4.31
86	47.7	8.11	5.06	8.18	5.18

A comparison of smoothing the image after the solid angle function and smoothing it before using a contrast phantom measurement is shown in Figure 7.2 with the same example used in Figure 7.2. In Figure 7.2 (b), it appears that the total image counts is higher when using the solid angle technique. This effect is caused by the way the image gets displayed. As discussed previously the images are scaled with respect to the maximum pixel value before getting displayed. With the regular reconstruction, the maximum pixel is always situated in the noise on the edge of the images. Consequently, the central part of the images is scaled down. Using the solid angle technique reduces the noise on the edge of the images and the maximum pixel value is found in the central part of the images. In figure 7.2, C_{PEM} increased by 11 %, and SNR improved by 13 %. The image quality improvement is significant, the hot-spot is much more visible and the background is still at a low level.

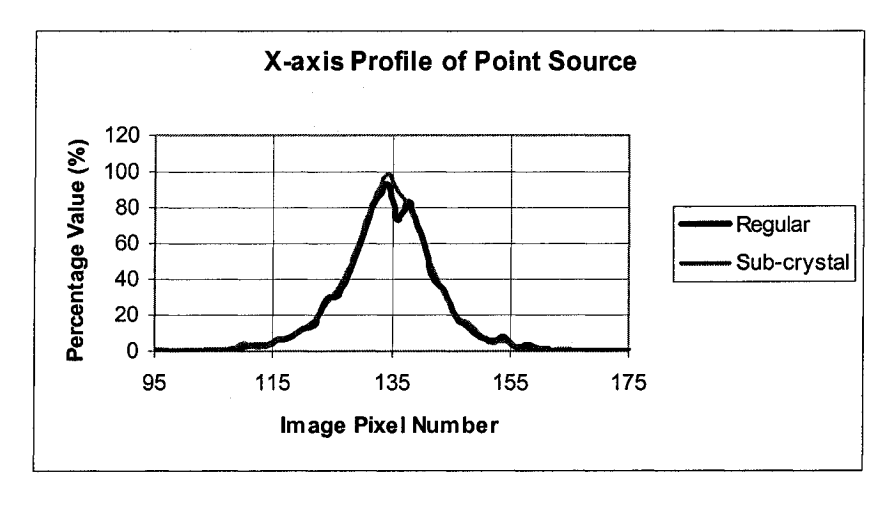
Table 7.2 shows the C_{PEM} and SNR for a range of true contrast. For all values of C_{TRUE} , the C_{PEM} decreased on average by 12 % but the SNR increased on average by 10 %.

Table 7.2 PEM contrast and SNR obtained for a set of projected contrast using the regular and the solid angle technique.

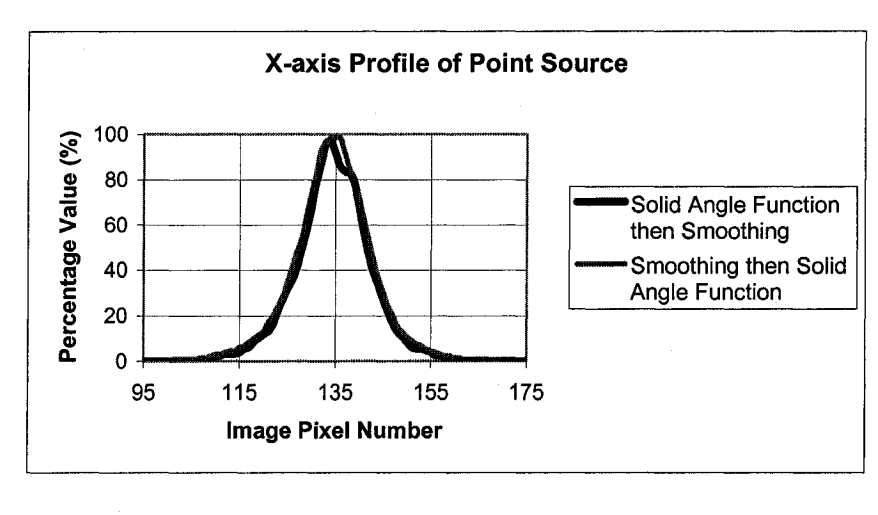
			Smoothed after the Solid Angle		l before the Angle
True Contrast C _{TRUE}	Projected Contrast C _{PROJ}	PEM Contrast C _{PEM}	SNR	PEM Contrast C _{PEM}	SNR
10	5.6	1.80	3.40	1.61	3.84
19	10.5	3.03	4.54	2.65	5.17
47	26.1	5.46	5.67	4.74	6.18
86	47.7	9.91	6.58	7.71	6.99

7.2 Point Source Measurements

Profiles comparing our two techniques are shown in Figure 7.3. The profiles were taken across the point source. Figure 7.3 (a) shows the comparison of the regular and the sub-crystal identification technique. The peak of that profiles across the peak of the point source was chosen at a point where sampling artifacts was predominant. The profile obtained with the sub-crystal identification profile is much smoother and free of the artifact. Figure 7.3 (b) shows the comparison of the regular and the solid angle technique. Again, the solid angle technique exhibits a smoother profile. Other results obtained with the point source positioned at different distance from one detector are shown in Table 7.3 and Table 7.4. The profiles obtained with the sub-crystal identification showed an improvement of both the spatial resolution and the noise increasing for point source closer to one detector. It was previously discussed that the planes located closer to one detector were more affected by the undersampling artifact, hence the sub-crystal identification improves noise more for point source located close to one detector. On the other hand the solid angle technique slightly deteriorated both the spatial resolution and noise.



(a)



(b)

Figure 7.3 Profiles across a point source. (a) shows the comparison between the regular and the sub-crystal identification. (b) shows the comparison between the regular smoothed technique and the solid angle technique.

Table 7.3 Spatial resolution and noise obtained for a set of projected contrast using the regular and the sub-crystal identification.

	Regular Identification		Sub-Crystal Identification	
Point Source Distance from Detector (cm)	Spatial Resolution (FWHM in mm)	Noise (Mean Square Difference)	Spatial Resolution (FWHM in mm)	Noise (Mean Square Difference)
3.0	3.94	1.50	3.87	1.24
2.0	4.05	3.70	3.96	2.40
1.5	4.32	3.50	4.11	3.07
1.0	4.61	2.32	4.70	1.73

Table 7.4 Spatial resolution and noise obtained for a set of projected contrast using the regular and the solid angle technique.

	Smoothed after the Solid Angle		gle Smoothed before the Soli	
Point Source Distance from Detector (cm)	Spatial Resolution (FWHM in mm)	Noise (Mean Square Difference)	Spatial Resolution (FWHM in mm)	Noise (Mean Square Difference)
3.0	3.94	0.44	4.08	1.87
2.0	4.06	0.98	4.23	1.33
1.5	4.32	0.75	4.45	0.80
1.0	4.88	0.87	5.53	1.60

7.3 Clinical Trial Replay

Figure 7.4 illustrates a replay of one of the 10 patients that was positively diagnosed as having a cancerous tumor using the PEM images. Three different reconstruction techniques are shown where the seven virtual image planes onto which the LORs are back-projected are also shown. Figure 7.4 (a) shows the regular image reconstruction. Figure 7.4 (b) shows the sub-crystal identification image reconstruction. In Figure 7.4 (c) the images were smoothed before the solid angle function. Using Figure 7.4 (a), the patient was diagnosed as having an invasive carcinoma. A significant focal uptake is visible. Both the sub-crystal identification technique and the re-ordering technique show a better contrast. The tumor definition is improved and the diagnosis is easier to make.

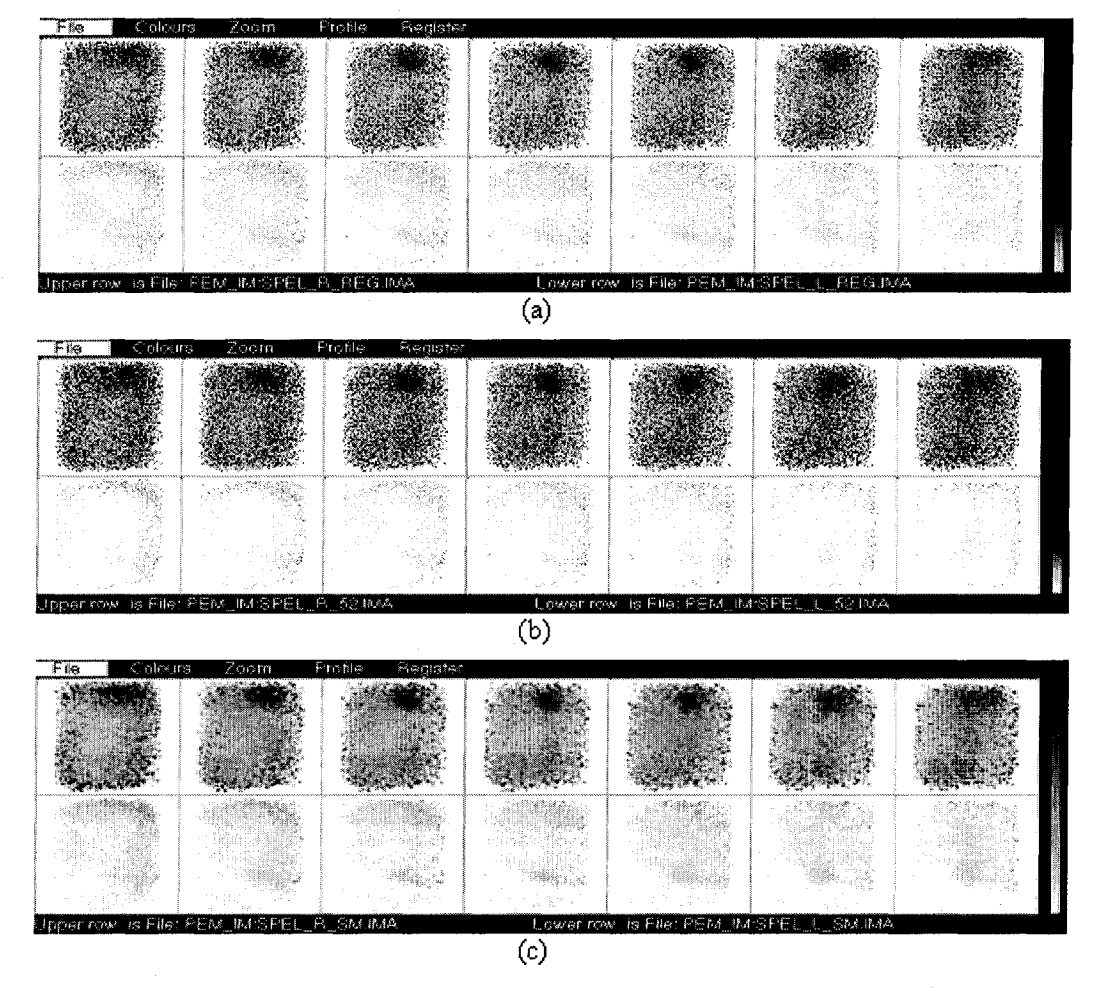


Figure 7.4 Images of a true positive patient reconstructed using different techniques. The top row of each image represents the suspected breast with breast cancer and the bottom row represents the contra-lateral breast with the same processing. The images were reconstructed with the regular crystal identification (a), using the sub-crystal identification (b). In (c) the images were smoothed before the solid angle function was applied.

Figure 7.5 shows illustrate a replay of one of the 3 patients that were diagnosed as having a cancerous tumor not using visual inspection but using count asymmetry. The sub-crystal identification technique (Figure 7.5 (b)) doesn't show any improvement but the re-ordering technique does (Figure 7.5 (c)). For that special case only, the contrast was improved from 1.26 (Figure 7.5 (a)) to 1.99 (Figure 7.5 (c)).

Contrast of the four true-negative patients was the same within a few percent. No hot-spot was found visualizing the two false-negative patients.

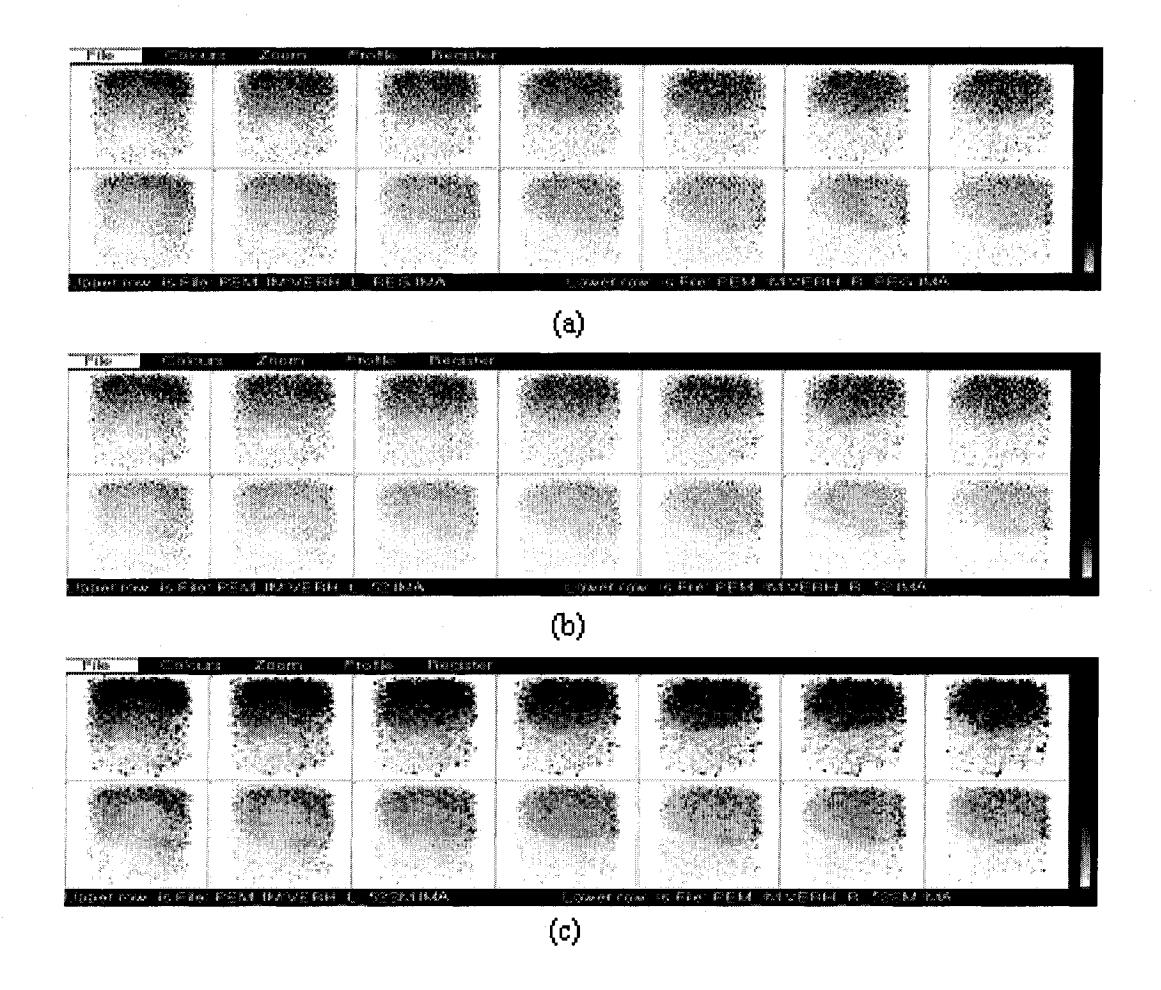


Figure 7.5 Images of a true positive patient reconstructed using different techniques diagnosed with count asymmetry. The top row of each image represents the suspected breast with breast cancer and the bottom row represents the contra-lateral breast with the same processing. The images were reconstructed with the regular crystal identification (a), using the sub-crystal identification (b). In (c) the images were smoothed before the solid angle function was applied.

7.4 ROC Curve Analysis

The ROC curves obtained form six medical physics students are shown in Figure 7.6. The ROC curves were obtained by plotting the sensitivity as a function of 1-specificity for different cut points. Since the diagnostic test was arranged using five test values, four points per curve were calculated. The dashed curves, obtained using the new reconstruction, tend to be closer to the left upper corner which depicts a higher accuracy test. The dotted lines, on the other hand, tend to be located closer to the pure guess line (thick solid line). There is even one case where the ROC curve goes over the pure guess line but then under, which is strange. There is another case where the curve lies almost directly on the pure guess line. It turns out that those two

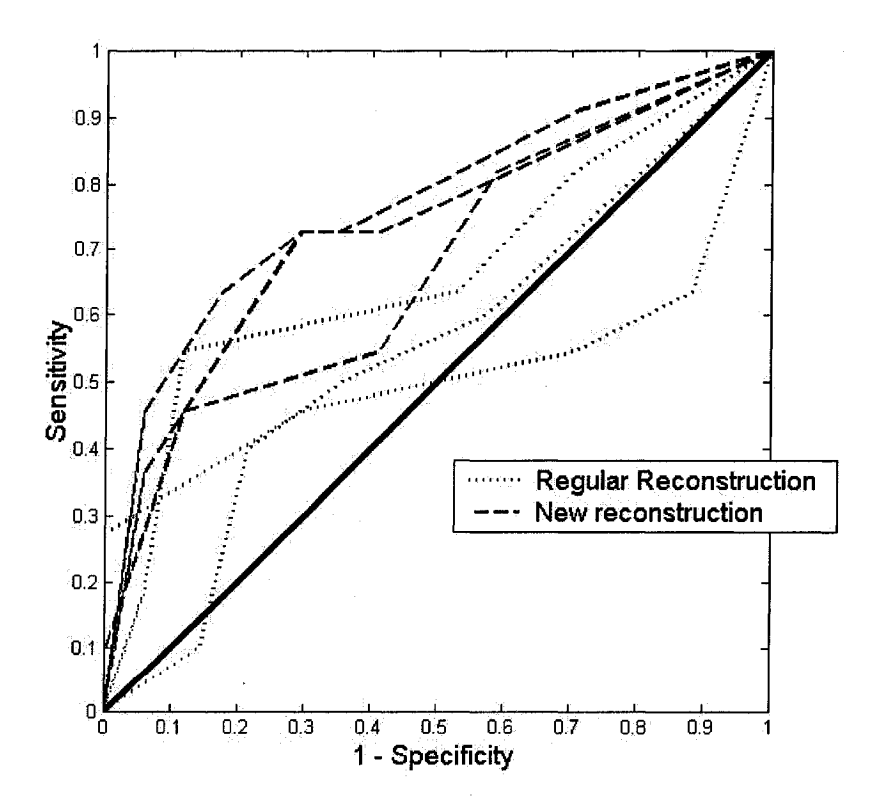


Figure 7.6 ROC curves from six medical physics students. The dotted curves were obtained with the regular reconstruction and the dashed curves from the new reconstruction, i.e. the sub-crystal identification and the solid angle techniques.

students were giving data whose file names had been mixed during the randomization of the data. For that reason, those two ROC curves were exclude in the cumulative ROC curve shown in Figure 7.7. The dashed ROC curve is made from three students whereas the dotted curve was obtained from only one student. The accuracy or areas under the curve, for the two tests are shown in table 7.5. Despite the low statistical significance of the results, there is a noteworthy improvement in accuracy of 6.4 % from the regular to the new reconstruction.

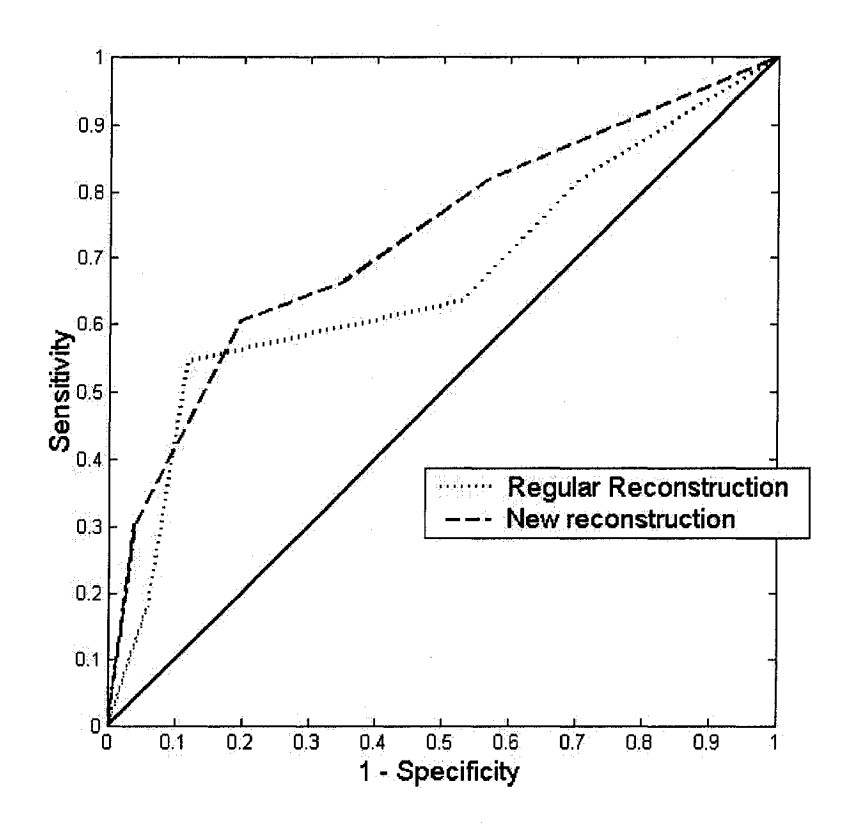


Figure 7.7 Cumulative ROC curves.

Table 7.5 Accuracy for the two reconstruction techniques.

	Accuracy (%)
Regular Technique	66.6
Sub-Crystal Identification and Solid Angle Techniques	73 ± 4

CHAPTER 8

Discussion and Conclusion

This document is a report of what we've accomplished during one year of research at the Montreal Neurological Institute in the research lab of Professor Christopher J. Thompson. Part of the first, the second, and the third chapters are describes the basic elements of PET and PEM. These chapters were essential in my understanding of PET from the basic physical principles to the display of a color image on a computer screen. This knowledge will certainly serve me all along my career has a medical physicist.

The fourth, fifth, and sixth chapters describe the core of the project. The project was related to the images obtained with the PEM scanner which was designed and built by Dr Thompson and his group before my arrival in the lab. The idea of the project started from the fact that the quality of the images obtained with the PEM scanner was poorer than expected. The images had a lower contrast and a higher noise amplitude than expected. The noise also seemed to have a certain grid like pattern overlaid on the images. Two techniques were investigated to improve image quality with respect to signal-to-noise and contrast for PEM system using a back-projection reconstruction method.

The first technique was related to the sampling artifact observed in most of the images. These artifacts come from the non-uniformity of the LORs crossing each image pixel. The number of LORs crossing an image pixel is dependent on the image pixel position, the size of the crystal and number of crystal elements; and it can vary drastically from one pixel to the other. The sub-crystal identification technique was developed in order to change the way the crystal was sampled and reduce the sampling artefact. The sub-crystal identification technique allows the LORs start and end points to shift within a crystal element towards the second most probable crystal element where the light appears to come from. The sub-crystal identification technique reduces sampling artifacts. The tube of response (TOR) allocation method, where tubes the size of the crystal elements are back-projected instead of lines, has also been proposed to reduce sampling artifacts [53]. But unlike the tube of response allocation method which reduces sampling artifact at the expense of image contrast, the sub-crystal identification technique reduces sampling artifacts and improves image contrast. The sub-crystal identification technique also improves SNR, and spatial resolution. But even if the image quality improved using the sub-crystal identification technique, the images didn't look too much different. The technique's effect was similar to a regular smoothing filter without the unavoidable loss in image quality due to the low-pass filtering.

The second technique was related to the high noise amplitude observed in the periphery of most of the images. The re-ordering technique which consists of re-

ordering the solid angle function and the smoothing algorithm reduced the noise in the peripheral regions of the image. It also increased the dynamic range of the image; hence improving SNR at the expense of image contrast. However, a loss in spatial resolution and an increase in noise were observed when using point source measurements. We argue that the increase in FWHM and noise is due to the fact that we used a relative 8 bits scale (1-256) to make our analysis. Since the dynamic range is changed, the point source appears noisier and wider increasing the noise and the FWHM, respectively.

Clinical trial image contrast of true-positive patients improved. One true-positive patient that was diagnosed only using count asymmetry between the two breasts, however asymmetry in the image was observed when using the re-ordering technique.

The image asymmetry of true-negative between the two breasts stayed relatively the same when using the two techniques.

The image quality improvement from the two techniques was not enough to directly improve accuracy and sensitivity of PEM-I, i.e. no diagnosis was changed.

An ROC curve analysis was performed on the clinical trial data to quantify the accuracy improvement of the PEM-1 detector. Out of six medical physics students, four actually did the test correctly. The others were given data that had been name

improperly. Going through the task of organizing the test was interesting and not obvious. I had to decide which images to use as training, who would be the examiners, the number of examiners and the number of test values to use. The accuracy or area under the ROC curve, improved by about 6 % for images reconstructed with both the sub-crystal identification and the solid angle techniques compared with images reconstructed with the regular technique. That improvement in accuracy is suspect from the limitation of the study. First, medical physics students were used rather than trained viewers. The test was also limited by the number of images used for the training. The reason was that the actual set was made out of 14 images, showing more images for the training had a direct impact of the number of images left for the actual study. Lastly, the size of the data set was probably the biggest limitation. The lack of predictive power from the small number of data sets was of great concern. Those limitations made the improvement in accuracy, and hence the clinical utility of our new techniques, quite questionable. I think that a larger data set of patients would have made the result be more significant.

APPENDIX

```
%
%
            Line of response density for planar detector
%
             Developed by Martin Hinse in March 2004
%
% This Matlab program calculates the line of response densities for
% a n_det x n_det single layer detector for 7 n_pix x n_pix equally
% distant image planes of located in between the two detectors. From
% geometry the LOR densities are calculated for only 4 planes.
% The output is four 3-D histogram of each of the four planes.
%
% f is the factor that determines the crystal identification
% technique used. For a regular crystal identification technique f
% is set to 1 and for a sub-crystal identification one can set f to
% 0.25 in order to get 4 lines of response per crystal element.
%
% x1 gets outputted for each iteration.
clear
n \det = 10;
n pix = 20;
ratio = n pix/n det;
f = 1
% Image matrix
lor dens = zeros(n pix, n pix, 4);
% Using lots of for loops even if I have was told many times not to.
for x1 = 1:f:n det
  x1
  for y1 = 1:f:n det
    for x2 = 1:f:n det
       for y2 = 1:f:n det
  % Find the slope of the line of response
         delta x = (x2 - x1);
         delta y = (y2 - y1);
  % Find the position in each image planes
            for i = 1:4
```

REFERENCES

- 1. "National Cancer Institute of Canada: Canadian Cancer Statistics 2003, Toronto, Canada, 2003." April 2003, ISSN 0835-2976.
- 2. E. Sickles, "Breast masses: mammographic evaluation," *Radiology*, vol. 173, pp. 297–303, 1989.
- 3. D. Kopans and S. Feig, "False positive rate of screening mammography," *N Engl J Med*, vol. 339, pp. 562–564, 1998.
- 4. D. Kopans, "The positive predictive value of mammography," *Am J Roentgenol*, vol. 158, pp. 521–526, 1992.
- 5. J. Meyer, T. Eberlein, P. Stomper, and M. Sonnenfeld, "Biopsy of occult breast lesions. Analysis of 1261 abnormalities," *JAMA*, vol. 263, pp. 2341–2343, 1990.
- 6. D. Henson, and L. Ries, "Progress in early breast cancer detection", *Cancer*, vol. 65, pp. 2155-2158, 1990.
- 7. N. Lang, N. Talbert, and K. Shewmake, "The current evaluation of non-palpable breast lesions," *Arch Surg*, vol. 122, pp. 1389-1391, 1987.
- 8. V. Jackson, R. Hendrick, S. Feig, and D. Kopans, "Imaging of radio-graphically dense breast," *Radiology*, vol. 188, pp. 297-301, 1993.
- 9. N. Avril, M. Schelling, J. Dose, W. Weber, and M. Schwaiger, "Utility of PET in breast cancer," *Clin Positron Imaging*, vol. 2, pp. 261-271, 1999.
- 10. N. Avril, C. Rose, M. Schelling, J. Dose, W. Kuhn, S. Bense, et al., "Diagnostic role of breast imaging with positron emission tomography and fluorine-18 fluorodeoxyglucose: use and limitations," *J Clin Oncol*, vol. 18, pp. 2495-3502, 2000.
- 11. K. Scheidhauer, A. Scharl, U. Pietrzyk, R. Wagner, U Gohring, K. Schomatcker, et al., "Qualitative F-18 FDG positron emission tomography in primary breast cancer: clinical relevance and practicability," Eur J Nucl Med, vol. 23, pp. 618-623, 1996.
- 12. L. Adler, J. Crowe, N. al-Kaisi, and J. Sunshine, "Evaluation of breast masses and axillary lymph nodes with [F-18]2-deoxo-2-fluoro-D-glucose PET," *Radiology*, vol. 187, pp. 743-750, 1993.
- 13. R. Wahl, R. Cody, G. Hutchins, E. Mudgett, "Primary and metastatic breast carcinoma: initial clinical evaluation with PET with the radiolabeled glucose analogue 2-[F-18]-fluoro-2-deoxy-D-glucose," *Radiology*, vol. 179, pp. 765–770, 1991.
- 14. N. Tse, C. Hoh, R. Hawkins, M Zinner, M. Dahlbom, Y. Choi, et al., "The application of positron emission tomographic imaging with fluoro-deoxyglucose to the evaluation of breast disease," *Ann Surg*, vol. 216, pp. 27–34, 1992.

- 15. O. Nieweg, E. Kim, W. Wong, W. Broussard, S Singletary, G. Hortobagyi, etal., "Positron emission tomography with fluorine-18-deoxyglucose in the detection and staging of breast cancer", *Cancer*, vol. 71, pp. 3920-3925, 1993.
- 16. D. Bruce, N. Evans, S. Heys, G. Needham, H. BenYounes, P. Mikecz, et al., "Positron emission tomography: 2-deoxy-2-[18F]-fluoro-D-glucose uptake in locally advanced breast cancers," *Eur J Surg Oncol*, vol. 21, pp. 280-283,1995.
- 17. D. W. Townsend, J. P. Carney, J. T. Yap, and N. C. Hall, "PET/CT Today and Tomorrow," *J Nucl Med*, vol. 45, pp. 4S-14S, 2004.
- 18. T. Beyer, D. W. Townsend, T. Brun, P. E. Kinahan, M. Charron, R. Roddy, et al., "A combined PET/CT scanner for clinical oncology," *J Nucl Med*, vol. 41, pp. 1369-1379, 2000.
- 19. D. W. Townsend, T. Beyer, P. E. Kinahan, T. Brun, R. Roddy, R. Nutt, et al. "The SMART scanner: a combined PET/CT tomograph for clinical oncology," *Nuclear Science Symposium*, 1998. Conference Record. 1998 IEEE, vol. 2, pp.1170 1174, 1998.
- 20. P. E. Kinahan, D. W. Townsend, T. Beyer, and D. Sashin, "Attenuation correction for a combined 3D PET/CT scanner", *Med Phys*, vol. 25, pp. 2046-2053, 1998.
- 21. W. Moses, T. Budinger, R. Huesman, and S. Derenzo, "PET camera designs for imaging breast cancer and axillary node involvement," *J Nucl Med*, vol. 36, no. 5, p. 69P, 1995.
- 22. R. Freifelder and J. Karp, "Dedicated PET scanners for breast imaging," *Phys Med Biol*, vol. 42, pp. 2463-2480, 1997.
- 23. N. Doshi, Y. Shao, R. Silverman, and S. Cherry, "Design and evaluation of an LSO PET detector for breast cancer imaging," *Med Phys*, Vol 27, pp. 1535-1543, 2000.
- 24. J. L. Robar, C. J. Thompson, K. Murthy, R. Clancy and A. M. Bergman, "Construction and calibration of detector for high-resolution metabolic cancer imaging," *Nucl Instr Meth Phys Res A*, vol. 392, pp. 402-406, 1997.
- 25. N. Zhang, C. J. Thompson, C. L. Thompson, and K. Nguyen, "Improving the performance of small planar detector for dedicated PET instruments," *IEEE Trans Nucl Sci.*, vol. 49, pp. 111-115, 2002.
- 26. C. Thompson, K. Murthy, Y. Picard, I. Weinberg, and R. Mako, "Positron emission mammography (PEM): a promising technique for detecting breast cancer," *IEEE Trans Nucl Sci*, vol. 42, pp. 1012-1017, 1995.
- 27. R. Huesman, G. Klein, W. Moses, "List-mode maximum likelihood reconstruction applied to positron emission mammography (PEM) with irregular sampling," *IEEE Trans Med Imaging*, vol. 19, pp. 532-537, 2000.

- 28. W. Moses and J. Qi, "Fundamental limits of positron emission mammography," *Nucl Inst Meth Phys Res*, vol. 497, pp. 82-89, 2003.
- 29. L. Adler, R. Freimanis, N. Lesko, S. Bergman, K. Geisinger, E. Levine et al., "Initial clinical results for FDG breast imaging with a dedicated PET camera," *J Nucl Med*, vol. 42, pp. 81P, 2001.
- 30. I. Weinberg, S. Majewski, A. Weisenberger, A. Markowitz, L. Aloj, L. Majewski et al., "Preliminary results for positron emission mammography: Real-time functional breast imaging in a conventional mammographic gantry," *Eur J Nucl Med*, vol. 23, pp. 804-806, 1996.
- 31. K. Murthy, M. Aznar, C. Thompson, A. Loutfi, R. Lisbona, and J. Gagnon, "Results of preliminary clinical trials of the positron emission mammography system PEM-I: a dedicated breast imaging system producing glucose metabolic images using FDG," *Jour Nucl Med*, vol. 41, pp. 1851-1858, 2000.
- 32. S. R. Cherry, J. A. Sorenson, M. E. Phelps, Physics in Nuclear Medicine, third edition, Saunders, Philadelphia, USA, 2003.
- 33. A. M. Bergman, C. J. Thompson, K. Murthy et al., "Technique to obtain positron emission mammography images in registration with x-ray mammograms," *Med Phys*, vol. 25, pp. 2119-2129, 1998.
- 34. E. B. Podgorsak, Review of radiation oncology physics: a handbook for teachers and students, International Atomic Energy Agency, Educational Report Series, 2003.
- 35. C. L. Melcher, "Scintillation crystals for PET," *J Nucl Med*, vol. 41, pp. 1051-1055, 2000.
- 36. G. F. Knoll, Radiation detection and measurement, Third Edition, John Wiley & Sons, Michigan, USA, 2000.
- 37. J. Sorenson and M. Phelps, Physics in Nuclear Medicine, Second Edition, W. B. Saunders Company, Philadelphia, USA, 1987.
- 38. S. D. Benedetti, C. Cowan, W. R. Konneker, and H. Primakoff, "On the Angular Distribution of Two-Photon Annihilation Radiation," *Phys Rev*, vol. 77, pp. 205-212, 1950.
- 39. N. Tomic, "The origin of the block effect which blurs images in positron emission tomography," Master's thesis, McGill University, Medical Physics Unit, 2003.
- 40. W.W. Moses and S.E. Derenzo, "Empirical observation of resolution degradation in positron emission tomagraphs utilizing block detectors," *J Nucl Med*, vol. 34, pp. 101P, (abstract) 1993.
- 41. C. J. Thompson, K. Murthy, I. N. Weinberg, and F. Mako, "Feasibility study for positron emission mammography," *Med Phys*, vol. 21, pp. 529-538, 1994.

- 42. R. R. Raylman, S. Majewski, R. Wojcik, A. G. Weisenberger, B. Kross, V. Popov, and H. A. Bishop, "The potential role of positron emission mammography for detection of breast cancer. A phantom study," *Med Phys*, vol. 27, 1943-1954, 2000.
- 43. Doshi, N.K.; Silverman, R.W.; Shao, Y.; Cherry, S.R., "maxPET, a dedicated mammary and axillary region PET imaging system for breast cancer," *IEEE Trans Nucl Sci*, vol. 48, pp. 811-815, 2001.
- 44. R. Freifelder, C. Cardi, I. Grigoras, J. R. Saffer, J. S. Karp, "First results of a dedicated breast PET imager, BPET, using NaI(Tl) curve plate detectors," *IEEE Nuclear Science Symposium Conference Record*, vol. 3, pp. 1241 1245, 2001.
- 45. Y. Picard and C.J. Thompson, "Determination of the centroid of interaction of the crystals in block detectors for PET," *IEEE Trans Nucl Sci*, vol. 41, pp. 1464-1468, 1994.
- 46. C. J. Thompson, C. J. Moreno, and Y. Picard, "PETSIM: Monte Carlo simulation of all sensitivity and resolution parameters of cylindrical positron imaging systems," *Phys Med Biol*, vol. 37, pp. 731-749, 1992.
- 47. Q. Jinyi, C. Kuo, R. H. Huesman, G. J. Klein, W. W. Moses, B. W. Reutter, "Comparison of rectangular and dual-planar positron emission mammography scanners," *IEEE Trans Nucl Sci*, vol. 49, pp. 2089-2096, 2002.
- 48. K. Murthy, C. J. Thompson, I. N. Weinberg, F. M. Mako, "Measurement of the coincidence response of very thin BGO crystals," *IEEE Trans Nucl Sci*, vol. 41, pp. 1430-1435, 1994.
- 49. K. Murthy, D. Jolly, M. Aznar, C. Thompson, P. Sciascia, A. Loutfi et al., "Quantification in positron emission mammography (PEM) with planar detectors: contrast resolution measurements using a custom breast phantom and novel spherical hot-spots," *IEEE Trans Nucl Sci*, vol. 46, pp. 2192-2196, 1999.
- 50. C. E. Metz, "ROC methodology in radiologic imaging," *Invest Radiology*, vol. 21, pp. 720-733, 1986.
- 51. J. A. Hanley and B. J. McNeil, "The meaning and use of the area under a receiver operating characteristic curve," *Radiology*, vol. 143, pp. 29-36, 1982.
- 52. J. A. Swets, "ROC analysis applied to the evaluation of medical imaging techniques," *Invest Radiol*, vol. 14, pp. 109-121, 1979.
- 53. M.F. Smith, S. Majewski, A. G. Weisenberger, D. A. Kieper, R. R. Raylman, T. G. Turkington, "Analysis of factors affecting positron emission mammography (PEM) image formation," *IEEE Trans Nucl Sci*, vol. 50, pp. 53-59, 2003.